Langtaosha (LTS) Preprint doi: https://doi.org/10.65215/LTSpreprints.2026.11.14.000387. This version posted November 14, 2026. The copyright holder for this preprint (which was not certified by peer review) is the author/funder. All Rights Reserved. No reuse allowed without permission.

Broad sensory expression and selective functional roles of *Ir25a* in the malaria mosquito *Anopheles stephensi*

Zi Ye[1, 2 †], Guanzhen Fan[2,3 †], Stephen T. Ferguson[2,4 †], Dan Gou[2,4], Yinna Wang[2,4], Shunfeng Li[5, 6], Shuang Xu[1], Ling Zhang[1], Heng Zhang[2,4], Zhiyue Lv[5, 6#], Feng Liu[2, 4 #]

1. School of Life Sciences, Guizhou Normal University, Guiyang, China
2. Institute of Infectious Diseases, Shenzhen Bay Laboratory, Shenzhen, China
3. School of Pharmaceutical Science and Technology, Faculty of Medicine, Tianjin University, Tianjin, China.
4. Guangdong Provincial Key Laboratory of Infection Immunity and Inflammation, Shenzhen, China
5. Key Laboratory of Tropical Disease Control (Sun Yat-sen University), Ministry of Education, Guangzhou, Guangdong, China
6. Provincial Engineering Technology Research Center for Biological Vector Control, Zhongshan School of Medicine, Sun Yat-sen University, Guangzhou, Guangdong, China

[†]Equal contribution
[#]Correspondence: liufeng@szbl.ac.cn; lvzhiyue@mail.sysu.edu.cn

Langtaosha (LTS) Preprint doi: https://doi.org/10.65215/LTSpreprints.2026.11.14.000387. This version posted November 14, 2026. The copyright holder for this preprint (which was not certified by peer review) is the author/funder. All Rights Reserved. No reuse allowed without permission.

Abstract

Mosquitoes rely heavily on their peripheral nervous system to sense various cues during host-seeking and blood-feeding. Ionotropic receptors (IRs) are a family of chemosensory receptors that play fundamental roles in mosquito chemical and physical cue detection. Among the three IR coreceptors, Ir25a is the most evolutionarily ancestral and conserved, whereas its function remains poorly understood, particularly in *Anopheles* mosquitoes. In this study, we integrated transgenic fluorescent labeling, single-nucleus RNA-seq (snRNA-Seq), electrophysiology, and behavioral assays to determine the functions of Ir25a in *An. stephensi*, an urban malaria vector. We found that *Ir25a* is broadly expressed in sensory neurons of multiple appendages in both female and male mosquitoes, including the antennae, maxillary palps, labella, and tarsi. Notably, Ir25a is localized in both CO_2-sensing and odor-sensing neurons in the maxillary palps. Detailed snRNA-Seq profiling further supports extensive co-expression of Ir25a with CO_2-sensitive gustatory receptors (GRs) and odor-sensitive odorant receptors (ORs) in chemosensory neurons, while also delineating accessory cell types not previously characterized in mosquito snRNA-seq. Surprisingly, *Ir25a* mutants display minimal changes in peripheral chemical responses in both antennae and maxillary palps. In contrast, *Ir25a* mutants exhibit severe thermosensory deficits, reduced CO_2 -evoked takeoff, complete abolishment of host-seeking and blood-feeding, along with reduced mating success. Taken together, this study systematically characterizes the broad expression of *Ir25a* and identifies its selective functional roles in sensory physiology, as well as the profound impact on host detection in the malaria mosquito *An. stephensi,* contributing to our long-term effort in *Anopheles* mosquito control and malaria prevention.

Keyword: Ionotropic receptor 25a, single-nucleus RNA-seq, gene editing, electrophysiology, host-seeking

Langtaosha (LTS) Preprint doi: https://doi.org/10.65215/LTSpreprints.2026.11.14.000387. This version posted November 14, 2026. The copyright holder for this preprint (which was not certified by peer review) is the author/funder. All Rights Reserved. No reuse allowed without permission.

Introduction

To locate blood meals, mosquitoes must decode a combination of carbon dioxide, host odors, heat, and visual cues into coordinated orientation and landing behavior. Host-seeking and blood-feeding behaviors are therefore the outcome of integrating information from multiple sensory pathways rather than a response to any singular stimulus acting alone[1]. Notably, disruption of these synergistic sensory pathways can lead to unexpected consequences. In *Aedes aegypti*, for example, loss of odorant-receptor signaling can enhance attraction to human skin temperature through compensatory changes in thermosensation[2]. Understanding sensory organization is particularly important for *Anopheles stephensi* (Diptera: Culicidae), a major urban malaria vector whose public health threat has been highlighted by its recent designation by the World Health Organization as an invasive species in Africa[3]. Its successful expansion across the continent has been driven by its remarkable ecological adaptability and the effects of climate change[4,5]. Central to its success as a disease vector are its acute sensory systems, which governs crucial host-seeking behaviors and facilitates reproduction. The molecular components underlying these sensory pathways are therefore compelling subjects for investigation, as their disruption may affect vector transmission behaviors in ways that cannot be predicted from responses to individual stimuli alone. Establishing how these shared components connect peripheral stimulus detection to coordinated behaviors could reveal both the flexibility of mosquito host seeking and potential vulnerabilities for its disruption.

Insect peripheral olfaction begins in sensory appendages, including the antennae and maxillary palps, where olfactory sensory neurons (OSNs) extend their dendrites into hair-like cuticular structures called sensilla[6]. These multicellular sensory units comprise trichogen and tormogen cells that form the sensory shaft and socket, while the glia-like thecogen cells ensheath the neurons[7,8]. Beyond providing structural integrity, these cells also maintain the ionic and chemical environment of the sensillum lymph by secreting proteins, such as odorant-binding proteins (OBPs), that modulate odor responses[9]. Experiments in *Drosophila melanogaster* have demonstrated altered sensory responses following thecogen-cell ablation, indicating that peripheral sensory function relies on interactions between neuronal and non-neuronal components[10]. While support cells surround the sensory dendrites, glial cells additionally ensheath the neuronal axons[11].

Within this cellular environment, chemical detection involves three major chemoreceptor families: odorant receptors (ORs), gustatory receptors (GRs), and ionotropic receptors (IRs)[12]. Insect ORs form heteromeric ligand-gated ion channels composed of an odor-sensitive tuning receptor and a conserved coreceptor Orco[13,14]. ORs have been shown to detect a wide variety of chemical classes, such as alcohols, aldehydes, ketones, and aromatic compounds, which notably encompass host-associated cues such as 1-octen-3-ol and indole[15]. GRs constitute an evolutionarily-related seven transmembrane receptor family that includes sugar- and bitter-sensitive receptors, as well as specialized receptors mediating the detection of carbon dioxide in mosquito palpal neurons[16,17]. IRs, by contrast, are evolutionarily related to ionotropic glutamate receptors (iGluRs), and play pleiotropic roles in olfaction, gustation, thermosensation, and hygrosensation in insects[18,19].

Conventionally, these chemosensory receptors were believed to occupy distinct neural circuits, with individual OSNs expressing just one of the major chemoreceptor classes; however, genetic mapping and single-nucleus transcriptomics have revealed co-

Langtaosha (LTS) Preprint doi: https://doi.org/10.65215/LTSpreprints.2026.11.14.000387. This version posted November 14, 2026. The copyright holder for this preprint (which was not certified by peer review) is the author/funder. All Rights Reserved. No reuse allowed without permission.

expression of multiple chemoreceptor families within individual olfactory neurons[20–22]. Such co-expression can have distinct functional consequences: *Aedes aegypti* palpal cpB neurons combine Orco-dependent responses to 1-octen-3-ol with amine responses that depend on Ir25a in many, but not all, recorded neurons[20,23]. Nevertheless, transcript co-localization alone neither establishes the composition of functional receptor complexes nor determines which responses require which specific component. Recent mosquito cell atlases further illustrate the diversity of receptor combinations while emphasizing the need for functional validation[24]. Therefore, linking these molecular combinations to defined cellular populations and stimulus-dependent phenotypes is essential to elucidate how shared sensory components orchestrate olfactory function.

Among the IRs, three highly conserved coreceptors have been identified: Ir8a, Ir25a, and Ir76b. Importantly, these three IR coreceptors show distinct functional diversification. Ir8a, as the first characterized IR coreceptor in mosquitoes, is involved in olfactory responses to acids[25]. Ir76b, on the other hand, regulates amine detection and may also participate in blood tasting and mating[26]. Ir25a is particularly notable for its broad neuronal distribution. In *Drosophila*, genetic mapping identified Ir25a expression in 88% of olfactory sensory neuron classes, including 82% of Orco-positive classes and all classes in the maxillary palps[21]. In *An. coluzzii*, antennal mapping similarly revealed extensive overlap with other IR coreceptors[22]. Mutagenesis of *Ir25a* has revealed deficits in olfactory responses to amines[27] and gustatory responses to salt and acids[28–31]. Ir25a, therefore, plays an important role in functional olfactory receptor machinery.

The functions of Ir25a also extend beyond olfaction. In *Drosophila*, it acts with Ir93a and additional IRs to detect cooling and moisture[32–34]. In *Aedes* mosquitoes, Ir25a plays essential roles in both olfactory responses to human volatiles and thermosensation [2,20,35]. Ir25a-dependent temperature sensing also supports synchronization of circadian rhythms to daily temperature cycles, linking peripheral sensory input to temporal organization of behavior[32]. More recent work has implicated Ir25a in pharyngeal detection of ingested carboxylic acids, extending its established gustatory roles to internal feeding-associated sensory pathway[36]. In *Bactrocera dorsalis*, Ir25a disruption reduced mating success and oviposition[37]. Taken together, these findings motivate investigating Ir25a as a versatile component shared across chemical and physical sensory pathways, whose disruption may affect essential behaviors in the mosquito life cycle, such as host-seeking.

The maxillary palp provides a tractable system for investigating how a broadly expressed coreceptor contributes to distinct sensory responses. In female *An. gambiae*, capitate peg sensilla house three molecularly and physiologically distinguishable OSNs, providing a stereotyped organization accessible to electrophysiological interrogation[17]. The cpA neuron co-expresses *Gr22*, *Gr23*, and *Gr24* and responds to carbon dioxide, whereas cpB and cpC neurons express *Orco* together with *Or8* and *Or28*, respectively[38]. These OR-associated pathways have different response profiles. Or8 confers high sensitivity to 1-octen-3-ol, while Or28 responds to a broader range of odorants, especially thiazoles[17]. In *An. stephensi*, transcriptomic analysis of mouthparts, including the maxillary palps and proboscis, similarly detected these OR and GR transcripts alongside *Ir25a* and *Ir76b*, and functional characterization confirmed the sensitivity of its Or8 ortholog to 1-octen-3-ol[39]. However, these tissue-level profiles do not resolve how *Ir25a* expression is distributed among individual sensory neurons and associated non-neuronal populations, nor do they establish which

Langtaosha (LTS) Preprint doi: https://doi.org/10.65215/LTSpreprints.2026.11.14.000387. This version posted November 14, 2026. The copyright holder for this preprint (which was not certified by peer review) is the author/funder. All Rights Reserved. No reuse allowed without permission.

palpal responses require it. Therefore, combining cell-resolved transcriptional profiling with spatial localization and physiological analysis offers a means to contextualize Ir25a within the cellular organization of this appendage and test its contribution to responses mediated by distinct receptor systems.

In this study, we combined CRISPR/Cas9-generated reporter and knockout lines with single-nucleus RNA sequencing, electrophysiology, and behavioral assays to relate the cellular distribution of Ir25a to its sensory and behavioral functions in *An. stephensi*. Genetic labeling revealed widespread expression across sensory appendages, while single-nucleus profiling of female maxillary palps resolved neuronal and non-neuronal populations and identified Ir25a enrichment across chemosensory neuron classes associated with both GR- and OR-mediated detection. Despite this broad distribution, Ir25a disruption selectively altered peripheral odor responses, including reduced palpal responses to amines while preserving measured CO_2 responses in cpA neurons. Nevertheless, mutant females exhibited reduced CO_2-evoked activation, markedly impaired heat attraction and host-directed landing, and lower insemination rates. Together, these findings distinguish the widespread deployment of a shared sensory coreceptor from the selective dependence of individual responses on its function. They further establish Ir25a as a critical contributor to host-seeking and reproductive success in this malaria vector, highlighting that its behavioral impact is not predictable directly from its expression pattern or responses to individual stimuli alone.

Results

Localization of AsteIr25a in the chemosensory neurons of mosquito

The olfactory appendages of *Anopheles* mosquitoes—antennae, maxillary palps, and labella—are covered with olfactory sensilla, each housing sensory neurons. To determine where *AsteIr25a* is expressed within the antennae, maxillary palps, and labella, we employed the binary Q-system, which uses a QF2 transcriptional factor driver and a QUAS-element effector to drive GFP expression in target cells[40]. Specifically, we generated a QF2 driver line (AsteIr25a-QF2) by CRISPR-mediated homologous recombination, inserting a 'T2A-QF2-3×P3-DsRed' cassette in-frame into the 10th exon of *AsteIr25a*, precisely replacing the stop codon (**Fig. 1A**)[20]. This driver carries a red-fluorescent marker in the compound eyes for visual screening, and its integrity was verified by genomic sequencing. The QUAS-GFP effector line, containing a randomly integrated 15×-QUAS-mCD8:GFP-3×P3-ECFP cassette, exhibits cyan fluorescence in the eyes. Crossing the driver with the effector produced progeny (*AsteIr25a*-QF2>QUAS-mCD8:GFP), enabling us to map sensilla that house *AsteIr25a*-expressing neurons via GFP labeling.

In the antenna, the primary olfactory organ, diverse sensillar types respond to distinct chemical stimuli. We found that *AsteIr25a* is broadly expressed across all olfactory sensilla types in female *An. stephensi*, including short and long trichoid sensilla (**Fig. 1B, C**), basiconic sensilla (also known as grooved pegs; **Fig. 1B, C**), and coeloconic sensilla (**Fig. 1D, E**). This widespread distribution suggests AsteIr25a may participate in detecting compounds from multiple chemical classes. The maxillary palp, by contrast, is a much simpler sensory appendage, housing only one sensillar type—capitate pegs (CP)—each containing one CO_2 -sensitive neuron and two additional neurons expressing OR/Orco. Notably, AsteIr25a was detected in all three CP neurons

Langtaosha (LTS) Preprint doi: https://doi.org/10.65215/LTSpreprints.2026.11.14.000387. This version posted November 14, 2026. The copyright holder for this preprint (which was not certified by peer review) is the author/funder. All Rights Reserved. No reuse allowed without permission.

across the 2nd, 3rd, and 4th palp segments (**Fig. 1F-H**), implying a role in both CO_2 and other odor detection. Consistent with previous reports of Ir25a involvement in *Drosophila* gustation[28–31], we observed substantial expression of *AsteIr25a* in the labella and tarsi of *An. stephensi*. In the labella, AsteIr25a appeared in both gustatory T1 sensilla and olfactory T2 sensilla (**Fig. 1I**). In the tarsi, expression was widespread in many neurons of the pro- , meso-, and metatarsi, but we also noted distinctive arrays of AsteIr25a-positive sensilla specifically on the 3rd (**Fig. 1J, K**) and 4th (**Fig. 1L, M**) segments of the protarsi.

Male *An. stephensi* displayed similar *AsteIr25a* expression patterns as females. As expected, males bear olfactory sensilla only on the two distal flagellomeres (12th and 13th) in the antennae, and our labeling confirmed *AsteIr25a* expression in short/long trichoid and basiconic sensilla restricted to these segments (**Fig. 1N, O**). In male maxillary palps, all three CP neurons were GFP- positive in the 4th segment (**Fig. 1P, Q**), and both T1 and T2 sensilla in the labella were also GFP-labeled (**Fig. 1R**).

Single-nucleus RNA sequencing resolves neuronal and non-neuronal populations in the female maxillary palp

To further establish the cellular context of *Ir25a* expression in the female maxillary palp, we analyzed single-nucleus RNA sequencing data from the female *An. stephensi* maxillary palps. Following quality-control filtering and the removal of predicted doublets, 9,268 nuclei were retained for analysis. To assess the sensitivity of the inferred populations to clustering parameters, we compared clusters across neighborhood sizes (k) and Leiden resolutions. To determine an appropriate neighborhood size, we performed a parameter sweep using k values 5, 10, 15, 20, 25, 30, 35, 40, 45, 50, 55, and 60 against resolution values of 0.25, 0.50, 0.75, and 1.00 (**Supplementary Fig. S1A, B**). A neighborhood size of $k = 50$ yielded the highest mean agreement with its two adjacent tested values across the four examined resolutions (mean adjusted Rand index = 0.947) and was used for all downstream analyses. We then examined cluster membership stability across a larger range of 16 resolutions, from 0.05 to 1.50 (**Supplementary Fig. S2**). The coarsest resolution—0.05—appeared to merge distinctive epithelial- and glial-like nuclear populations. Across the full range of resolutions, many clusters remained stable both in terms of library membership and total number, whereas the finest resolution—1.50—mostly produced more epithelial-like sub-clusters without revealing substantial heterogeneity among the remaining clusters. We therefore elected to use a resolution of 0.70 as a useful, whole-dataset representation, partitioning major neuronal and non-neuronal cell-type populations and capturing heterogeneity within the epithelial populations without adopting every fine-scale subdivision observed at higher resolutions.

Our subsequent graph-based clustering with 50 neighbors (k) and a Leiden resolution of 0.70 resolved 16 transcriptomic clusters (**Fig. 2A, B**). We annotated clusters by integrating Wilcoxon-ranked marker genes with comparative orthology, protein-domain annotations, and phylogenetic placement of candidate chemoreceptors (**Supplementary Data 1**). A curated marker gene heatmap showed expression patterns across individual nuclei (**Fig. 2A**), while a complementary dotplot summarized mean log-normalized expression and the fraction of nuclei with at least one detected unique molecular identifier (UMI) for each selected gene (**Fig. 2C**). These analyses resolved chemosensory and mechanosensory neurons in addition to multiple support-cell and epithelial populations, together with glia, muscle, and hemocytes.

Langtaosha (LTS) Preprint doi: https://doi.org/10.65215/LTSpreprints.2026.11.14.000387. This version posted November 14, 2026. The copyright holder for this preprint (which was not certified by peer review) is the author/funder. All Rights Reserved. No reuse allowed without permission.

Three clusters exhibited receptor profiles consistent with the principal chemosensory neuron classes of the capitate peg. Notably, these assignments reflect the molecular identities consistent with capitate peg neurons, as opposed to physiologically derived classifications. Cluster 6 contained 193 nuclei and was enriched for the *Gr22*/*Gr23*/*Gr24* receptor signature, supporting its assignment as putative, CO_2-detecting cpA neurons (**Fig. 2A, C**). *Gr22*, *Gr23*, and *Gr24* were detected in 82.4%, 95.9%, and 71.0% of nuclei within this cluster, respectively. Clusters 10 and 13 contained 641 and 680 nuclei and were distinguished by preferential expression of *Or8* and *Or28*, respectively, in combination with *Orco*, supporting putative cpB and cpC identities. *Or8* was detected in 98.1% of nuclei in cluster 10, whereas *Or28* was detected in 97.5% of cluster 13. All three capitate peg clusters showed expression of *abnormal chemosensory jump 6* (*acj6*), while the two odorant receptor neurons could be distinguished by an uncharacterized marker gene *ASTEI20_036852*. Moreover, cpC neurons could be distinguished from cpB neurons based on the presence of an ortholog of *Drosophila vermilion* (*v*), which encodes the heme-dependent enzyme tryptophan 2,3-dioxygenase (TDO), catalyzing the conversion of tryptophan to N-formylkynurenine in the kynurenine pathway[41]. In *Drosophila*, *vermilion* is best known for its role in ommochrome eye-pigment biosynthesis, although the kynurenine pathway also has broader metabolic and neuronal functions. A *vermilion*/TDO homolog has been experimentally characterized in *An. gambiae*[42], and the mosquito protein can rescue *Drosophila vermilion* mutant eye color, supporting conservation of its enzymatic activity[43]. The significance of its enriched expression in this palpal olfactory neuron population is presently unclear, however, and conservation of biochemical function does not necessarily imply conservation of its cell-type-specific physiological role.

A fourth neuronal population, cluster 8, was distinguished by *no mechanoreceptor potential C* (*nompC*) (**Fig. 2A, C**). This cluster contained 333 nuclei, with *nompC* detected in 84.1%, which we assigned as a putative mechanosensory neuron cluster. This cluster was additionally characterized by *decima* (*dcma*) and another uncharacterized gene *ASTEI20_038844*. Together, these four receptor-associated populations occupied distinct regions of the PaCMAP embedding (**Fig. 2B**).

The non-neuronal clusters included several transcriptionally distinguishable support-cell populations. Clusters 0, 1, and 15 contained 706, 828, and 61 nuclei, respectively, and all three shared prominent *Sox15* expression (**Fig. 2A-C**), consistent with a provisional assignment as tormogen/socket cells[44,45]. Despite this shared signature, the clusters differed in their expression of additional curated marker genes, including *angiotensin converting enzyme* (*Ance7*), *Vajk1*, and selected odorant-binding (OBPs) and chemosensory proteins (CSPs). *Ance7* was particularly informative for cluster 0, whereas *Vajk1* was a prominent marker of cluster 15. Cluster 5, containing 697 nuclei, was distinguished by *Prospero (pros*) and *nompA* and was assigned a thecogen identity[46]. The corresponding transcripts were detected in 81.8% and 42.6% of cluster 5, compared with only 3.1% and 1.0% in the remaining nuclei (**Fig. 2A, C**).

Although the support-cell marker profiles supported tormogen- and thecogen-like assignments, no population could be confidently identified as trichogen cells. Examination of the predicted *artichoke* (*atk*) ortholog, *ASTEI20_044372*, which has been reported as a potential trichogen cell marker gene in Drosophila[46] did not reveal a discernible cluster-specific expression pattern that could support this assignment (**Supplementary Fig. S3**). Indeed, *atk* was only detected in 2 out of 9,268 nuclei (0.02%). However, two additional populations were retained under descriptive

Langtaosha (LTS) Preprint doi: https://doi.org/10.65215/LTSpreprints.2026.11.14.000387. This version posted November 14, 2026. The copyright holder for this preprint (which was not certified by peer review) is the author/funder. All Rights Reserved. No reuse allowed without permission.

support-cell labels. Cluster 3 contained 714 nuclei and was distinguished by *sodium-coupled monocarboxylate transporter 1* (*SCMT1*), *follistatin* (*Fs*), *cyclic-AMP response element binding protein A* (*CrebA*), and *kon-tiki* (*kon*). This profile broadly supported a distinct support-like population but could not be associated with a named subtype. Therefore, we used the label "Unresolved Support Cell". Cluster 11 contained 282 nuclei and showed strong expression of *hormone receptor 38* (*HR38*), *cyclic nucleotide-gated ion channel subunit A* (*CngA*), *5-hydroxytryptamine receptor-like* (*5HT1A-like*), and *dysfusion* (*dysf*) (**Fig. 2A, C**). Additional predicted cuticular proteins in its broader marker gene set, including *ASTEI20_038350* and *ASTEI031065*, supported a cuticle-associated interpretation. We consequently used the label "Cuticle Support Cell".

Epithelial-like populations comprised the largest recovered set of nuclei. Clusters 2, 4, and 7 contained 1,321, 465, and 1,978 nuclei, respectively, totalling 3,764 nuclei, or 40.6% of the dataset (**Fig. 2C**). All three clusters shared a *grainyhead* (*grh*) expression profile, with additional expression of *oskyddad* (*osy*)[24,47]. Cluster 4 was further distinguished by an uncharacterized gene, *ASTEI20_033036*, which was detected in 95.7% of its nuclei. The three populations occupied neighboring regions of the PaCMAP embedding, with greater intermingling than other, more isolated neuronal and non-neuronal populations (**Fig. 2B**). We therefore retained the common epithelial annotation while acknowledging their unique heterogeneity within individual cluster identities.

Our analysis also recovered several, less abundant populations, which nevertheless displayed strong, characteristic marker gene signatures. Cluster 14 contained 44 nuclei and was assigned a glial identity on the basis of *reverse polarity* (*repo*) and *myoglianin* (*myo*) expression. These transcripts were detected in 65.9% and 63.6% of the cluster, respectively (**Fig. 2A, C**). Cluster 12 comprised only 16 nuclei but exhibited a distinctive muscle-like profile, including *myosin light chain* (*Mlc2*), *obscurin* (*Obsc*), *myosin heavy chain* (*Mhc*), and *troponin I* (*TnI*). *Mlc2* and *Obsc* were detected in 13 and 15 of these nuclei, respectively, while *Mhc* and *TnI* were each detected in 14, supporting its identification as muscle-derived nuclei despite their small size. Cluster 9 contained 309 nuclei and was distinguished by *papilin* (*PPN*), *peroxidasin* (*Pxn*), *secreted protein, acidic, cysteine-rich* (*SPARC*), and *Nimrod B2* (*NimB2*), supporting a hemocyte identity.

Together, these marker profiles and embedding analyses distinguished both prominent and rare neuronal and non-neuronal populations recovered from the female maxillary palp, in addition to several distinctive but uncertain support populations lacking a decisive subtype assignment. This atlas establishes a cellular framework for examining the distribution of *Ir25a* transcripts and their co-detection with other receptor gene signatures.

AsteIr25a is enriched across GR- and OR-associated chemosensory populations

Having established the major palpal cell populations, we next examined the distribution of *AsteIr25a* transcripts within this cellular landscape. Mapping log-normalized expression onto the same PaCMAP embedding revealed a concentration of *AsteIr25a* signal in the putative cpA, cpB, and cpC populations, with more scattered detection elsewhere (**Fig. 3A**). To quantify this distribution while accounting for differences in cluster size, we counted nuclei containing at least one *AsteIr25a* UMI in each cluster (**Fig. 3B**). *AsteIr25a* was detected in 133 of 193 cpA-associated nuclei (68.9%), 350 of 641 cpB-associated nuclei (54.6%), and 367 of 680 cpC-

Langtaosha (LTS) Preprint doi: https://doi.org/10.65215/LTSpreprints.2026.11.14.000387. This version posted November 14, 2026. The copyright holder for this preprint (which was not certified by peer review) is the author/funder. All Rights Reserved. No reuse allowed without permission.

associated nuclei (54.0%). By contrast, detection was lower in the mechanosensory population, occurring in 35 of 333 nuclei (10.5%), and in the remaining clusters combined, only 216 out of 7,421 nuclei contained an AsteIr25a UMI (2.6%). The low-frequency detection in other populations may be due to technical artifacts or could represent real but rare expression outside the primary chemosensory populations. Taking the localization and single-nucleus sequencing data together, these observations support enrichment in chemosensory populations, but perhaps not exclusive restriction to chemosensory cells. Either way, the single-nucleus analysis establishes *AsteIr25a* in multiple co-expression contexts within the heterogeneous palpal tissue of *An. stephensi* mosquitoes.

We next examined whether *AsteIr25a* transcripts were co-expressed in the same nuclei alongside the receptor marker genes signatures used to characterize these populations (**Fig. 3C**). For cpA-associated nuclei, the comparison signature was defined by the detection of at least one CO_2-detecting GR. For cpB- and cpC-associated nuclei, the signature was defined by the detection of *Orco* or the corresponding tuning OR, *Or8* or *Or28*, respectively. Each nucleus was then assigned to one of four categories: marker gene signature only (P), signature co-expressed with *Ir25a* (P+I), *Ir25a* only (I), or neither detected (-). All percentages were calculated relative to the full population represented in each panel. Under these detection rules, all nuclei in the three capitate peg chemosensory clusters contained at least one marker gene transcript. Every *AsteIr25a*-positive nucleus in these populations was therefore co-expressed with a chemoreceptor (**Fig. 3C**). The remaining 31.1% of cpA-, 45.4% of cpB-, and 46.0% of cpC-associated nuclei did not have a detectable level of *Ir25a* transcript. Thus, *AsteIr25a* appears to be co-expressed in both GR and OR neurons, rather than merely occurring in separate nuclei that happen to cluster together with these chemoreceptor-positive nuclei in aggregate.

The comparison populations showed a different co-detection pattern. In the mechanosensory cluster, 74.8% of nuclei contained *nompC* without *AsteIr25a*, whereas only 9.3% contained both (**Fig. 3C**). Among these nuclei, 1.2% contained *AsteIr25a* without a detectable level of *nompC*, and 14.7% contained neither *nompC* nor *Ir25a*. For the remaining pooled clusters, each nucleus was evaluated against the rank-1 Wilcoxon marker gene signature of its own assigned cluster. Within this pool, 74.8% contained their cluster-specific marker without a detectable level of *AsteIr25a*, 2.2% contained both, 0.7% contained *AsteIr25a* without the assigned marker, and 22.2% contained neither. The pooled percentages describe all nuclei in those clusters, rather than an equally weighted average across clusters.

Together, these analyses identify *AsteIr25a* transcript co-detection across the three receptor-defined chemosensory populations in this preparation, with lower-frequency detection in other palpal populations. These observations provide the cellular context for subsequent physiological analyses, but the precise receptor-complex assembly remains unknown.

AsteIr25a knockout affects antennal olfactory sensitivity

To explore the functional role of *AsteIr25a* in chemosensation, we generated a null mutant by inserting a 3×P3-DsRed fluorescent marker into the 4th exon via CRISPR-mediated homology-directed repair (**Fig. 4A**). Mutants were selected by eye fluorescence and confirmed by sequencing. Homozygous *AsteIr25a* mutants (*Ir25a*$^{-/-}$; 11.1 ± 0.16 days) developed at a similar rate to wild-type (WT; 10.75 ± 0.22 days) and heterozygotes (*Ir25a*$^{+/-}$; 10.95 ± 0.18 days) during the larval stage (**Fig. 4B**).

Langtaosha (LTS) Preprint doi: https://doi.org/10.65215/LTSpreprints.2026.11.14.000387. This version posted November 14, 2026. The copyright holder for this preprint (which was not certified by peer review) is the author/funder. All Rights Reserved. No reuse allowed without permission.

However, the pupal stage of *Ir25a*$^{-/-}$mutants (36.17 ± 0.11 h) was significantly prolonged compared to the other two genotypes (WT: 34.06 ± 0.29 h; *Ir25a*$^{+/-}$: 34.86 ± 0.17 h) (**Fig. 4C**). Additionally, female adult longevity was markedly reduced in knockouts relative to WT females (**Fig. 4D**), hinting broader physiological roles for *AsteIr25a* beyond olfaction.

We then assessed antennal responses of homozygous mutant females to a panel of human-related odors spanning diverse chemical categories. Unlike the drastic EAG reduction seen in mosquito *Orco* knockouts[48,49], *AsteIr25a* mutation caused significant changes for only four compounds: α-pinene (WT: 0.176 ± 0.009 mV; *Ir25a*$^{-/-}$: 0.066 ± 0.007 mV), geranyl acetone (WT: 0.718 ± 0.082 mV; *Ir25a*$^{-/-}$: 0.260 ± 0.024 mV), 2-acetylthiazole (WT: 0.038 ± 0.026 mV; *Ir25a*$^{-/-}$: 0.299 ± 0.044 mV), and spermidine (WT: 0.289 ± 0.020 mV; *Ir25a*$^{-/-}$: 0.008 ± 0.013 mV) (**Fig. 5A**). Given the broad antennal expression of Ir25a yet only modest EAG effects, we performed single- sensillum recording (SSR) to examine responses at the neuronal level. SSR results aligned with EAG data, showing no significant genotype differences in either short sharp trichoid (SST) or short blunt trichoid sensilla (SBT) (**Supplementary Fig. S4A, B**).

AsteIr25a knockout selectively reduces maxillary palp odorant sensitivity

To evaluate the impact of Ir25a loss on palp sensory function, we measured electropalpogram (EPG) responses to ten compounds. Most tested chemicals evoked comparable EPG responses in wild-type and *Ir25a*$^{-/-}$ females; however, two amines—heptylamine (WT: 0.065 ± 0.011 mV; *Ir25a*$^{-/-}$: 0.017 ± 0.004 mV) and hexylamine (WT: 0.512 ± 0.074 mV; *Ir25a*$^{-/-}$: 0.310 ± 0.050 mV)—elicited significantly reduced responses after knockout (**Fig. 5B**), suggesting that certain amine-sensitive tuning IRs coexpress with AsteIr25a in palp OSNs.

Given that *AsteIr25a* localizes to all three CP neurons—one with a large spike (cpA) and two with smaller spikes (cpB/C)—we used SSR to interrogate neuronal responses to a chemical panel. CO_2 , 4,5-dimethylthiazole, 2-methyl-2-thiazoline, and pyridine specifically activated cpA neurons, with no differences between WT and *Ir25a*$^{-/-}$ females (**Fig. 5C**). In cpB/C neurons, while tested alcohols and ketones elicited similar responses across genotypes, heptylamine (WT: 59.3 ± 4.3 spikes/s; *Ir25a*$^{-/-}$: 16.0 ± 2.9 spikes/s) and hexylamine (WT: 173.3 ± 8.2 spikes/s; *Ir25a*$^{-/-}$: 67.0 ± 12.6 spikes/s) provoked markedly attenuated firing in the mutants (**Fig. 5D**), consistent with the EPG findings.

Abolished host-seeking and mating deficits in *AsteIr25a* null mutants

Mosquitoes rely on multimodal host cues—heat, CO_2 , and human odors—to locate a blood source. We therefore performed a series of behavioral assays to assess the contribution of AsteIr25a. In a heat-pod attraction assay, heat alone strongly attracted WT females (**Fig. 6A**). Both heterozygous and homozygous mutants, however, showed a dramatic reduction in heat attraction, with the homozygous response nearly abolished, underscoring an essential role for Ir25a in heat sensing (**Fig. 6A**). Furthermore, *Ir25a*$^{-/-}$ mutants exhibited significantly reduced CO_2 -induced takeoff activity compared to heterozygous and WT females (**Fig. 6B**), indicating that Ir25a contributes to CO_2 -evoked behavioral responses, even though the peripheral neuronal responses to CO_2 in the maxillary palps remained intact.

Langtaosha (LTS) Preprint doi: https://doi.org/10.65215/LTSpreprints.2026.11.14.000387. This version posted November 14, 2026. The copyright holder for this preprint (which was not certified by peer review) is the author/funder. All Rights Reserved. No reuse allowed without permission.

We next tested behavioral responses to live hosts using mice as the odor source, with a barrier preventing direct contact. Landing frequencies did not differ between WT and heterozygotes, but homozygous mutants completely lost landing activity (**Fig. 6C**). When the barrier was removed to allow direct contact and blood- feeding, WT and heterozygotes showed no difference in landing, whereas no landing events were observed in homozygous mutants (**Fig. 6D**). To confirm whether this insensitivity was mouse-specific, we repeated the assay with human hands. Strikingly, homozygous mutant females showed neither landing nor feeding on human hands, while both WT and heterozygotes displayed normal, active blood- feeding (**Fig. 6E**). Collectively, these data show that the null mutation of *AsteIr25a* completely abolishes host-seeking and blood-feeding behaviors in *An. stephensi*, correlating with deficits in both heat and host-odor sensation.

Given our prior work linking the ionotropic receptor Ir76b to mating behavior in *Anopheles*[26], we tested whether Ir25a affects female insemination. Newly eclosed virgin males and females were co-housed for free mating, and insemination rates were assessed by spermatheca dissection[26]. *Ir25a*$^{-/-}$ females had a significantly lower insemination rate than WT females (**Fig. 6F**), suggesting Ir25a also involves mate recognition.

Several studies have proposed transcriptional regulatory functions for chemosensory coreceptors[50–52]. To investigate whether Ir25a acts similarly, we performed Illumina RNA- seq on antennae from WT and *Ir25a*$^{-/-}$ females and compared chemoreceptor transcript abundances. In contrast to previous reports showing widespread transcriptional changes upon coreceptor loss, *Ir25a* null mutation did not alter the expression of any chemosensory receptors across the OR, IR, or GR families (**Supplementary Fig. S5A**). A parallel analysis in the maxillary palps yielded the same conclusion (**Supplementary Fig. S5B**).

Discussion

Mosquito host-seeking and reproductive behaviors depend on the coordinated activity of multiple sensory pathways, yet the contributions of individual receptor components to these complex processes remain incompletely understood. Here, we combined genetic labeling, single-nucleus transcriptomics, electrophysiology, and behavioral assays to investigate the distribution and functional roles of AsteIr25a in *An. stephensi*. We found that *AsteIr25a* is broadly expressed across sensory appendages and co-expressed with distinct chemoreceptor families within the maxillary palps. Despite this widespread distribution, disruption of AsteIr25a produced relatively selective changes in peripheral olfactory responses, contrasting sharply with the pronounced deficits in thermal attraction, host-seeking, blood-feeding, and mating behavior observed in mutant mosquitoes. Together, these findings highlight an important distinction between the anatomical distribution of a sensory receptor and its functional contributions, suggesting that the behavioral significance of Ir25a extends beyond its role in the detection of individual chemical stimuli.

Broad expression of *Ir25a* across mosquito chemosensory organs suggests diverse sensory functions

Ionotropic receptors have emerged as versatile sensory receptors that extend beyond canonical odor detection to regulate diverse modalities, including gustation, thermosensation, and hygrosensation. Here, using a CRISPR-mediated *AsteIr25a*-

Langtaosha (LTS) Preprint doi: https://doi.org/10.65215/LTSpreprints.2026.11.14.000387. This version posted November 14, 2026. The copyright holder for this preprint (which was not certified by peer review) is the author/funder. All Rights Reserved. No reuse allowed without permission.

QF2 reporter system, we demonstrate that *AsteIr25a* is broadly expressed throughout the major chemosensory organs of *An. stephensi*, including the antennae, maxillary palps, labella, and tarsi. This distribution resembles the widespread expression of *Ir25a* reported in *Drosophila*, *Aedes* and *Anopheles* mosquitoes[20–22,53,54], supporting an evolutionarily conserved role for this coreceptor in multiple sensory contexts. By employing this binary expression system, we not only mapped *Ir25a*-expressing neurons but also identified the specific sensillar subtypes they innervate, thereby establishing a cellular framework for functional dissection of Ir25a-mediated pathways.

Notably, the localization of *AsteIr25a* appears considerably more expansive than that previously described for *Ir76b* in *An. coluzzii*, which was confined largely to antennal coeloconic and basiconic sensilla[26]. In contrast, we observed *AsteIr25a* labeling across most antennal sensillar types and within all three neuronal populations of the maxillary palp capitate pegs.

Beyond these principal olfactory structures, we observed substantial *Ir25a* expression in gustatory neurons of the labella and tarsi, hinting pleiotropic roles in contact chemoreception. Intriguingly, we uncovered a distinct array of protarsal sensilla housing Ir25a-positive neurons, which aligns with a previous study describing *Ir25a*-expressing thermosensory neurons in the protarsi of *Aedes* mosquitoes[2]. This finding suggests that *Anopheles* may possess specialized tarsal neuronal arrays dedicated to heat and/or tastant detection. Together, these observations suggest that AsteIr25a participates in multiple sensory contexts, although its widespread anatomical distribution alone cannot establish the molecular receptor combinations or physiological functions of individual neurons. Resolving its expression within defined sensory cell populations is therefore an important step toward understanding its functional diversification.

Single-nucleus profiling reveals the cellular diversity of the *Anopheles stephensi* maxillary palp

Our single-nucleus analysis places *AsteIr25a* within the molecularly resolved cellular landscape of the female maxillary palp. Profiling 9,268 nuclei distinguished the principal chemosensory neurons in the capitate peg together with mechanosensory neurons, multiple support and epithelial clusters, and rarer glial, muscle, and hemocyte populations (**Fig. 2**). Consistent with our localization results, *AsteIr25a* transcripts were preferentially detected across the putative cpA, cpB, and cpC populations (**Fig. 3**), demonstrating that molecularly distinct neuronal identities can share common sensory components. This cellular atlas also provides candidate marker genes for investigating less well-characterized components of the palpal sensory system.

The expression profiles of the three chemosensory populations are consistent with the established organization of anopheline capitate peg sensilla. Molecular and physiological characterization of *An. gambiae* associated the CO_2 -sensitive cpA neuron with Gr22/Gr23/Gr24 and the neighboring cpB and cpC neurons with Or8 and Or28, respectively[17]. Subsequent mouthpart transcriptomics in *An. stephensi* identified these receptor transcripts and established the sensitivity of its Or8 ortholog to 1-octen-3-ol but did not assign the full tissue transcriptome to individual cell populations[39]. Our analysis extends that tissue-level framework by resolving the distinctive neuronal and non-neuronal populations within the maxillary palps.

Langtaosha (LTS) Preprint doi: https://doi.org/10.65215/LTSpreprints.2026.11.14.000387. This version posted November 14, 2026. The copyright holder for this preprint (which was not certified by peer review) is the author/funder. All Rights Reserved. No reuse allowed without permission.

The co-detection of *AsteIr25a* transcripts with GR-associated signatures in cpA neurons and OR-associated signatures in cpB and cpC neurons is consistent with growing evidence that chemoreceptor expression is not strictly segregated among neuronal classes. Extensive co-expression of major chemoreceptor families has been demonstrated in *Ae. aegypti*, *An. coluzzii*, and *D. melanogaster*[20–22], with recent single-nucleus analyses further revealing diverse receptor combinations across mosquito sensory appendages[24]. Our findings are consistent with this organization, extending now to the female *An. stephensi* maxillary palps.

Beyond the chemosensory neurons, we recovered several transcriptionally distinct populations consistent with tormogen and thecogen support cells (**Fig. 2**). Prominent *Sox15* signal across three populations supports their provisional identification as tormogen/socket cells, consistent with its established role in socket-cell differentiation in *Drosophila* mechanosensory organs[44]. Among the tormogen clusters, differences involving *Ance7*, *Vajk1*, and other accessory-protein markers suggest further heterogeneity that may reflect anatomical location, association with different sensory structures, or different physiological states. Similarly, a *pros*-enriched population, with additional *nompA* expression, supports a thecogen-associated identity[46]. Notably, pros was detected in 81.8% of nuclei within this population, compared with only 42.6% for *nompA*, consistent with recent evidence that *pros* may provide broader coverage of thecogen cells than the commonly used *nompA* reporter.

In contrast, trichogen support cells remained elusive. Although an *artichoke atk*-GAL4 reporter has recently been validated in *Drosophila* trichogen cells, the same study reported limited endogenous *atk* detection in adult antennal single-nucleus data[46]. We similarly detected the predicted *An. stephensi atk* ortholog, ASTEI20_044372, in only two of 9,268 nuclei (0.022%) (**Supplementary Fig. S3**). Another candidate, *Osi23/gore-tex*, has been functionally characterized during olfactory sensillum development rather than established as a universally detectable adult trichogen transcript[55]. These observations highlight the limitations of transferring developmental or reporter-based markers to adult transcriptomic datasets across species. Our sparse *atk* detection cannot distinguish failure to recover trichogen nuclei from limited transcript capture, stage- or tissue-dependent expression, or differences in marker suitability between flies and mosquitoes. However, given our apparent recovery of tormogen and thecogen candidates, it is tempting to speculate that our remaining unresolved and/or cuticle support clusters may in fact represent trichogen cells. The marker genes reported in this study therefore provide a compelling list of candidate genes for resolving this question.

Together, these findings extend the molecular description of the female *An. stephensi* maxillary palp beyond its principal chemoreceptor populations, revealing substantial non-neuronal diversity and providing candidate marker genes for future investigations. Linking these transcriptional identities to anatomical localization and cell-specific functional perturbations will be essential for determining how Ir25a contributes to distinct sensory pathways and how surrounding support cells influence their physiological functions.

Ir25a contributes selectively to peripheral olfactory responses despite widespread neuronal expression

Indeed, despite widespread expression across mosquito chemosensory neurons, *AsteIr25a* disruption produced significant electroantennographic changes for only a small subset of tested odorants, and individual sensillum responses remained largely

Langtaosha (LTS) Preprint doi: https://doi.org/10.65215/LTSpreprints.2026.11.14.000387. This version posted November 14, 2026. The copyright holder for this preprint (which was not certified by peer review) is the author/funder. All Rights Reserved. No reuse allowed without permission.

intact. This contrasts with the severe olfactory phenotype associated with disruption of Orco, which effectively silences conventional OR complexes[48,49,56]. Instead, our results align with previous work on Ir76b in *Anopheles*, reinforcing the view that these IR coreceptors make stimulus- and neuron-dependent contributions to sensory responsiveness, rather than a uniform requirement across all olfactory pathways[26].

In parallel with the findings in *Aedes*[20], we observed Ir25a labeling in all three neurons of capitate pegs, which implies the co-expression of *Ir25a* and *Orco* based on prior Orco mapping studies[48,57]. Functionally, AsteIr25a deletion significantly attenuated EPG and SSR responses to heptylamine and hexylamine in the cpB/C neuronal populations, consistent with earlier reports that Ir25a contributes to amine detection in mosquito palps. In *Ae. aegypti*, Ir25a mutants similarly showed reduced sensitivity to hexylamine and triethylamine[20]. Our findings extend this mechanism to *An. stephensi* and identify both heptylamine and hexylamine as stimuli strongly dependent on AsteIr25a. Interestingly, although we documented co-expression of IRs with GRs (in cpA neurons) and ORs (in cpB/C neurons) in the maxillary palp, eliminating Ir25a did not significantly diminish electrophysiological responses to CO_2 or other odors that typically engage GR/OR pathways. The functional relevance of GR/OR co-expression with *Ir25a* therefore remains enigmatic, a point also noted in prior investigations[20,21].

Interestingly, disruption of AsteIr25a did not significantly alter the transcript abundance of other chemoreceptors in either the antennae or maxillary palps, contrasting with reports of transcriptional changes following the loss of other chemosensory coreceptors[50,52]. This suggests that the selective olfactory deficits observed in *AsteIr25a* mutants are unlikely to result from widespread changes in chemoreceptor gene expression. Nevertheless, these bulk transcriptomic analyses cannot exclude changes in individual neuronal populations, receptor trafficking, or other molecular processes that may influence sensory function.

Loss of Ir25a disrupts thermal attraction and host seeking

Behavioral assays revealed the most pronounced phenotypic alterations in *Ir25a* mutants. Unlike *Aedes* mosquitoes that require CO_2 to gate heat-seeking behaviors[1], *An. stephensi* females exhibit robust attraction to a heat source alone, highlighting the primacy of thermal cues in anopheline host-seeking. Previous studies have shown that *An. stephensi* deploys multiple appendages to detect host-associated thermal stimuli[58], and thus the broad *Ir25a* expression we documented across these same structures provides a plausible anatomical substrate for such multimodal thermal detection.

Heat from a host is transferred via conduction, convection, and infrared radiation. Radiation is thought to be detected through the cation channel TRPA1, whereas ionotropic receptor complexes participate in other forms of thermal sensing[2,59–62]. In *Aedes*, *TRPA1* mutants retain thermotaxis toward a heat source but lose the ability to detect infrared radiation[63,64]. Our data place Ir25a as an essential component of the heat-seeking machinery in *Anopheles*, suggesting that anopheline thermal detection, like that of *Aedes*, is potentially mediated by parallel receptor systems: IR complexes involved in conductive/convective heat detection, and TRPA1 regulating preferred temperature range and radiation sensing.

Most dramatically, *Ir25a* null mutants exhibited complete abolition of host-seeking and blood-feeding in our behavioral assays. These behavioral phenotypes were considerably more pronounced than the peripheral olfactory deficits, suggesting that

Langtaosha (LTS) Preprint doi: https://doi.org/10.65215/LTSpreprints.2026.11.14.000387. This version posted November 14, 2026. The copyright holder for this preprint (which was not certified by peer review) is the author/funder. All Rights Reserved. No reuse allowed without permission.

the consequences of AsteIr25a loss cannot be explained solely by impaired detection of the individual odorants examined here. Given the severe reduction in thermal attraction, we hypothesize that Ir25a-dependent thermosensory pathways make a particularly important contribution to host recognition. We propose a model of anopheline host seeking in which volatile cues initiate flight activation and orientation, while thermal and contact cues become increasingly important during close-range approach, landing, and blood feeding. However, the relative contributions of these sensory modalities remain to be established, and additional experiments that independently manipulate host-associated cues will be necessary to determine whether impaired thermal detection is sufficient to explain the loss of host-seeking behavior.

Interestingly, CO_2 -induced takeoff was reduced in *Ir25a* mutants even though CO_2 responses of the cpA neuron in capitate pegs were preserved. This discrepancy suggests that Ir25a is not required for primary CO_2 transduction but may contribute to the integration of CO_2 with thermal or olfactory information, which has been reported in multiple studies[1,25,65]. Mosquito host seeking depends on interactions among CO_2, odor, and heat rather than on any single cue acting independently. Thus, although the primary CO_2 sensitivity of the capitate peg is preserved in *An. stephensi Ir25a* mutants, the reduced CO_2 -induced takeoff may reflect altered integration or downstream transformation of CO_2 signals within the broader host-seeking network, potentially as a consequence of impaired Ir25a-dependent thermal signaling.

Beyond host-seeking, AsteIr25a disruption was also associated with prolonged pupal development, reduced adult survival, and decreased insemination rates, suggesting broader consequences for mosquito physiology and reproduction. Previous studies have similarly implicated ionotropic coreceptors in reproductive behaviors, including Ir76b in *Anopheles* and Ir25a in *Bactrocera dorsalis*[26,37]. However, the mechanisms underlying these phenotypes remain unresolved. In particular, the contributions of male and female sensory function to the observed mating deficits have not been distinguished, while the reduced longevity of *AsteIr25a* mutants raises the possibility of broader physiological effects. Future studies employing tissue-specific perturbation and genetic rescue will therefore be important for separating direct sensory functions from secondary consequences of Ir25a loss.

Conclusions

Together, our findings suggest a model in which *Ir25a* is broadly deployed across sensory neurons but contributes selectively to their physiological functions, with its importance depending on the molecular and cellular context in which it operates. Within this framework, Ir25a-dependent thermal signaling may be particularly important for host recognition, such that disruption of a specific sensory modality can profoundly impair host-seeking and blood-feeding despite the preservation of many peripheral olfactory responses. The dissociation between intact peripheral CO_2 detection and diminished CO_2 -evoked behavioral activation further suggests that the contribution of individual sensory pathways to complex behaviors cannot necessarily be predicted from their responses to isolated stimuli. Future studies should seek to identify the molecular partners underlying Ir25a-dependent sensory responses, characterize the functions of Ir25a-positive neurons in different appendages, and employ cell-type-specific genetic perturbations to establish how these pathways

Langtaosha (LTS) Preprint doi: https://doi.org/10.65215/LTSpreprints.2026.11.14.000387. This version posted November 14, 2026. The copyright holder for this preprint (which was not certified by peer review) is the author/funder. All Rights Reserved. No reuse allowed without permission.

contribute to host-seeking and reproduction. The cellular atlas and candidate markers established here provide a foundation for such investigations, including the largely unexplored contributions of non-neuronal support cells. Ultimately, understanding how broadly expressed sensory components acquire specialized physiological functions, and how these functions are integrated to produce coordinated behaviors, may reveal new opportunities for disrupting mosquito host recognition and disease transmission.

Materials and Methods

Mosquito maintenance

The *Anopheles stephensi* strain was kindly provided by Dr. Jingwen Wang at Fudan University, Shanghai, China, and reared as previously described[26]. All mosquito lines were maintained in environmental chambers at 27˚C and 75% relative humidity under a 12:12 light-dark cycle and supplied with 10% sucrose water in the Shenzhen Bay Laboratory Insectary.

Single-nucleus RNA sequencing

Tissue collection. Maxillary palp collection for nucleus extraction was performed as previously described[20,47]. 40-50 5-8-day-old non-blood-fed female *An. stephensi* were anesthetized at 4˚C and then placed in the 70 μm cell strainer (Falcon, 352350). The mosquitoes were gently rinsed with 5 mL ice-cold 100% ethanol and subsequently rinsed with 10 mL ice-cold Schneider's *Drosophila* Medium (Gibco, 21720024). The cell strainer with mosquitoes was placed into a 60 mm Petri dish on ice. 1 mL of ice-cold Schneider's *Drosophila* medium was added into the strainer to moisturize the mosquitoes. The maxillary palps were then removed using forceps and placed into a DNA LoBind 1.5 mL tube (Eppendorf, 022431021) with 300 μL Schneider's *Drosophila* Medium on ice. The dissection procedure was limited to 90 min to ensure nuclei integrity. The sample was then flash-frozen in liquid nitrogen and stored at −80°C until ready for nuclei extraction. A total of approximately 1000 maxillary palps were collected for nucleus extraction.

The samples were then processed to prepare a single-cell nuclei suspension based on the recommended method on the official platform of 10x Genomic (Pleasanton, USA) and Biomarker Technologies Corporation (Beijing, China). A microfluidic chip was used to generate gel beads in emulsion (GEMs), which encapsulate single-cell nuclei, reagents, and gel beads in oil droplets. Cell nuclei in the GEMs were lysed, and RNA was reverse-transcribed with primers containing a Cell Barcode and UMI. After the GEMs were broken, full-length cDNA was amplified by PCR before purification. The cDNA library was then sequenced using the Illumina NovaSeq 6000 platform at a sequencing depth of 50,000 reads per cell.

Single-nucleus data processing and quality control. CellRanger v7.0.0 was used to produce a filtered feature-barcode count matrix from one biological preparation of female *Anopheles stephensi* maxillary palps, which was subsequently analyzed in Python 3.14.7 using a workflow designed around Scanpy 1.12.4 and AnnData 0.13.3.post0[66]. The input contained 10,175 nucleus-associated barcodes and 12,687 unique gene features. Quality-control metrics were calculated for total unique molecular identifier (UMI) counts, the number of detected unique gene features, and the percentage of counts assigned to mitochondrial genes. Raw counts were $\log_2$-transformed, and nuclei were flagged when their values fell more than three normal-

Langtaosha (LTS) Preprint doi: https://doi.org/10.65215/LTSpreprints.2026.11.14.000387. This version posted November 14, 2026. The copyright holder for this preprint (which was not certified by peer review) is the author/funder. All Rights Reserved. No reuse allowed without permission.

719 consistency-scaled median absolute deviations (MADs) below the median. All zero
720 values were separately flagged as low-quality libraries. Nuclei with mitochondrial
721 counts exceeding a strict threshold of 5% were also flagged as low quality. Failure of
722 any quality-control metric resulted in exclusion from the dataset. These filters
723 removed 40 nuclei, leaving 10,135 for downstream doublet assessment
724 (**Supplementary Fig. S6A-C**).

725 Putative doublets were identified using Scanpy's implementation of Scrublet[67]. An
726 auxiliary UMAP was generated before removing putative doublets to visualize their
727 relationship to the full dataset (**Supplementary Fig. S6D**). This diagnostic used 3,000
728 highly variable genes (HVGs), 50 principal components, and a 15-neighbor graph.
729 Removing 867 predicted doublets left 9,268 nuclei for downstream analyses. All
730 12,687 input gene features were retained in the main analysis.

731 Expression normalization, feature selection, and principal component analysis. After
732 filtering, each nucleus library was normalized to a total of 10,000 counts, followed by
733 a natural-log transformation. HVGs were identified using Scanpy's analytic Pearson-
734 residual implementation. Genes were ranked by residual variance under a negative-
735 binomial offset model. The 3,000 highest-ranked genes were selected. Pearson
736 residuals were then recomputed from the count matrix restricted to those HVGs and
737 used for the principal component analysis (PCA). Fifty PCs were calculated from this
738 residual matrix using mean-centered PCA with the ARPACK solver.

739 **Neighborhood construction and parameter sensitivity.** Neighborhood graphs were
740 constructed from all 50 PCs using Euclidean distance and Scanpy's UMAP
741 connectivity kernel. Leiden community detection was performed on the weighted,
742 undirected connectivity graph using Scanpy with the igraph backend.

743 Neighborhood sensitivity to graph parameters was evaluated for k = 5, 10, 15, 20, 25,
744 30, 35, 40, 45, 50, 55, and 60. One graph was constructed for each k, and Leiden
745 clustering was performed at resolutions 0.25, 0.50, 0.75, and 1.00. At each resolution,
746 partitions were compared only between immediately adjacent tested k values using the
747 adjusted Rand index (ARI), implemented in scikit-learn 1.9.0. For each k, available
748 lower- and higher-neighbor ARIs were summed using their mean, median, minimum,
749 maximum, and population standard deviation (ddof=0). Interior values therefore had
750 eight contributing comparisons, whereas the two boundary values had four. The
751 centered-mean curve averaged both neighboring comparisons across all four
752 resolutions and was plotted only for interior k values (**Supplementary Fig. S1**). A
753 value of k = 50 was retained for the final graph.

754 **Resolution selection and membership visualization.** With k = 50 fixed for graph
755 construction, Leiden clustering was repeated at resolution 0.05 and at resolutions
756 0.10-1.50 in increments of 10, for a total of 16 tested resolutions. Relationships
757 between the solutions were examined using a custom Python visualization method
758 following a clustering-tree concept (**Supplementary Fig. S2**). Membership patterns
759 were considered together with marker gene profiles, and a resolution of 0.70 was
760 ultimately chosen to represent the data.

761 **PaCMAP visualization.** Two-dimensional embeddings were generated from the 50-
762 dimensional PCA representation using PaCMAP 0.9.1 (http://jmlr.org/papers/v22/20-
763 1061.html), selected for its design emphasis which improves on more traditional
764 UMAP and *t*SNE representations, capturing both local and broader-scale structure.
765 The implementation used 10 PaCMAP neighbors, a mid-near pair ratio of 0.5, a

Langtaosha (LTS) Preprint doi: https://doi.org/10.65215/LTSpreprints.2026.11.14.000387. This version posted November 14, 2026. The copyright holder for this preprint (which was not certified by peer review) is the author/funder. All Rights Reserved. No reuse allowed without permission.

further-pair ratio of 2.0, Euclidean distance, a learning rate of 1.0, and three optimization stages of 100, 100, and 250 iterations. PCA initialization, the FAISS neighbor-search backend, and internal PCA preprocessing (apply_pca=True) were used. PaCMAP's neighborhood parameter of 10 was independent of the $k = 50$ graph used for Leiden clustering, and cluster assignments were not inferred from the two-dimensional coordinates.

Marker genes and cell-type interpretation. Marker genes were ranked using the Wilcoxon rank-sum implementation in Scanpy with tie correction. This choice was informed by benchmark analyses showing strong performance for several simple approaches, including Wilcoxon-based marker selection[68]. The top 50 ranked genes per cluster were considered when assigning cluster identities. Curated heatmaps were then chosen from these marker profiles and additional genes of interest (**Supplementary Data 1**).

Reference gene models, protein-domain annotation, and orthology. Comparative annotation of *An. stephensi* genes relied on an integrative framework incorporating gene model predictions and protein sets for *An. stephensi* UCISS2018, *An. gambiae* PEST, *Ae. aegypti* LVP_AGWG, and *D. melanogaster* FlyBase release r6.68.

The *An. stephensi* predicted protein set was analyzed using InterProScan 6 workflow release 6.0.1 through Nextflow with the Docker profile and Gene Ontology and pathway mappings enabled (--goterms –pathways)[69]. InterProScan results were imported from JSON Lines output. Integrated InterPro entries, member database signature accessions, GO terms, and pathways were collected and aggregated across protein isoforms and linked to each predicted gene model. Orthogroups and pairwise orthology relationships were obtained using OrthoFinder[70]. Target orthologs were derived from the predicted orthology relationships, not from orthogroup membership.

Candidate chemoreceptor selection and phylogenetic placement. Candidate chemoreceptor proteins were selected from the *An. stephensi* reference protein set by matching any relevant InterProScan signatures, including IPR004117, PF02949, or PTHR21137 for ORs, IPR013604, PF08395, or PTHR21143 for GRs, and IPR019594, IPR001320, IPR001828, PF10613, PF00060, or PF01094 for IRs. The resulting sets contained 50 OR, 68 GR, and 113 IR/iGluR protein records, including isoforms.

Candidates were then placed against three annotated reference phylogenies. OR candidates were analyzed against an OR reference containing 1,360 sequences curated from iOrME v1.0[71]. This reference included *Acyrthosiphon pisum*, *An. gambiae*, *Apis mellifera*, *Blattella germanica*, *Calopteryx splendens*, *Camponotus floridanus*, *Cloeon dipterum*, *D. melanogaster*, *Manduca sexta*, *Nasonia vitripennis*, *Pediculus humanus*, and *Tribolium castaneum*. GR candidates were placed against 1,084 sequences derived from Mitchell, Moran, and McKenna (2026)[72]. IR/iGluR candidates were placed against a 457-sequence reference derived from Croset et al. 2010[54]. Each reference comprised an aligned protein dataset, a fixed tree, a fitted evolutionary-model, and sequence-associated annotation labels.

Reference alignments and phylogenies were constructed separately for the OR, GR, and IR/iGluR sequence collections described above. Within each collection, reference protein sequences were combined and aligned using MAFFT[73]. Alignment columns were subsequently trimmed using ClipKIT in smart-gap mode[74]. An amino-acid evolutionary model was selected for each trimmed reference alignment using the MOOSE model-selection procedure in RaxML-NG and the Bayesian information

Langtaosha (LTS) Preprint doi: https://doi.org/10.65215/LTSpreprints.2026.11.14.000387. This version posted November 14, 2026. The copyright holder for this preprint (which was not certified by peer review) is the author/funder. All Rights Reserved. No reuse allowed without permission.

criterion[75]. The candidate subsitution-model set comprised LG, WAG, JTT, Vt, BLOSUM62, DAYHOGG, DCMUT, JTT-DCMUT, Q.pfam, and Q.insect. The search considered equal-rate, gamma-distributed, and FreeRate models of among-site rate variation, with two to six categories permitted for FreeRate models. The best-fitting model identified by this search was retained for phylogenetic inference. Maximum-likelihood reference phylogenies were inferred using RaxML-NG under the selected models, with searches initiated from ten parsimony starting trees. The highest-likelihood topology was retained for each reference collection. Branch lengths and evolutionary-model parameters were then optimized on that topology using RaxML-NG's evaluation mode (--evaluate), with both model and branch-length optimization enabled (--opt-model on --opt-branches on). The resulting trimmed reference alignment, optimized reference tree, and fitted evolutionary-model file constituted the reference inputs for subsequent EPA-ng placement.

Query proteins were added to the corresponding reference alignment with MAFFT using --add, --keep_length, --amino, and --anysymbol. Evolutionary placement was performed using EPA-ng with the reference alignment, reference tree, aligned queries, and the reference's fitted RaxML-format model file supplied explicitly[76]. Placements were summarized by retaining the highest likelihood-weight-ratio placement for each protein and evidence run, with ties resolved by likelihood and then original placement order.

Gene naming conventions. The GFF-derived metadata, InterProScan annotations, OrthoFinder relationships, and phylogenetic placement results were organized into an SQLite database, and a gene-centric evidence table was exported with one row for every feature in the single-nucleus RNA sequencing expression matrix (**Supplementary Data 1**). Gene names were considered together with orthology and domain evidence. While this comprehensive integration of functional and orthologous evidence provided convenient naming conventions for graphing, reporting, and discussing various genes observed in the sequencing data, we note that domain-level annotations and orthology do not guarantee shared function across species.

Software and other sources. Analyses and figure generation were recorded in an Org-mode literate notebook using a persistent Python session in a Pixi-managed environment. In addition to the packages specified above, the reported environment included NumPy 2.5.3, pandas 3.0.5, SciPy 1.18.1, scikit-learn 1.9.0, igraph 1.0.0, PaCMAP 0.9.1, Matplotlib 3.11.1, and Seaborn 0.13.2.

The cartoon cell-type depictions in Fig. 2 were obtained from Sevier Medical Art, licensed under CC BY 4.0. These are meant to be colorful and illustrative; they are not a representation of the actual underlying biological cell structure.

Mosquito mutagenesis

Mosquito mutant lines were generated as previously described[26]. The CRISPR gene-targeting vector was the generous gift from the laboratory of Andrea Crisanti at Imperial College London, London, UK[77]. The single-guide RNA (sgRNA) sequence was designed using CHOPCHOP[78] to target the 4th exon of *AsteIr25a* gene (ASTEI20_043271.R60478). The complementary oligos (**Supplementary Data 2**) were synthesized (Sangon Biotech) and subcloned into the CRISPR vector by Golden Gate cloning (NEB, E1601S). The *3×P3-DsRed* homologous template was constructed based on the pHD-DsRed vector (Addgene plasmid #51434)[79], where the 1.5-2kb homologous arms extending either direction from the double-strand break

Langtaosha (LTS) Preprint doi: https://doi.org/10.65215/LTSpreprints.2026.11.14.000387. This version posted November 14, 2026. The copyright holder for this preprint (which was not certified by peer review) is the author/funder. All Rights Reserved. No reuse allowed without permission.

(DSB) site were PCR amplified with the custom oligonucleotide primers: Ir25a_PaqCI_F/Ir25a_PaqCI_R; Ir25a_SapI_F/Ir25a_SapI_R (**Supplementary Data 2**) and sequentially inserted into the PaqCI/SapI restriction sites of the vector. The *T2A-QF2-3×P3-DsRed* homologous template was constructed with Gibson Assembly (NEB, E5510S), in which the "*T2A-QF2-3×P3-DsRed*" element was amplified from the ppk301-T2A-QF2 HDR plasmid (Addgene plasmid# 130667)[80] and the 2kb homologous arms were PCR amplified with the primers: Ir25a_LArm_F/Ir25a_LArm_R; Ir25a_RArm_F/Ir25a_RArm_R (**Supplementary Data 2**). The T2A sequence was designed to insert in-frame to replace the stop codon.

The microinjection was conducted at Shenzhen Bay Laboratory Mosquito Gene Editing Service Center using a protocol following a previous study[26]. In brief, newly laid (~0.5-h-old) embryos of the wild-type *An. stephensi* were immediately collected and aligned on a filter paper moistened with 25 mM sodium chloride solution. The embryos were fixed on a coverslip with double-sided tape, and a drop of halocarbon oil 27 was applied to cover them. The coverslip was further fixed on a slide under a compound microscope with a 10× objective (Sunny Instruments, E5). Microinjection was performed using Femtojet 4i microinjector (Eppendorf) and aluminosilicate needles (Sutter Instrument, AF100-64-10) which were pulled on a Sutter P-1000 needle puller. The gene-targeting vector and the homologous template were co-injected at 300 ng/μL each. Injected embryos were subsequently placed in deionized water containing artificial sea salt (Instant Ocean; 0.3 g/L) and thereafter reared under normal Shenzhen Bay Laboratory insectary conditions.

First-generation (G0) injected adults were separated by sex and crossed to 5× wild-type sex counterparts. Their offspring (F1) were screened for DsRed-derived red eye fluorescence. Red-eyed F1 females were individually crossed to 5× wild-type males to establish a stable mutant line. DNA extraction was performed after reproduction using FastPure Cell/Tissue DNA Isolation Mini Kit (Vazyme Biotech, DC102), and PCR was performed to validate insertion of the fluorescence marker using primers spanning the DSB sites (**Supplementary Data 2**). PCR products were sequenced to confirm the accuracy of the genomic insertion. The heterozygous mutant lines were then back-crossed to the wild-type *An. stephensi* for at least five generations before putative homozygous individuals were manually screened for DsRed-derived red eye fluorescence intensity. Putative homozygous mutant individuals were mated with each other before being sacrificed for genomic DNA extraction and PCR analyses to confirm their homozygosity.

The effector line (QUAS-mCD8:GFP) was generated by co-injecting the pBAC-ECFP-15xQUAS_TATA-mcd8-GFP-SV40 plasmid (Addgene #104878)[57] with a pBac transposase helper plasmid[52]. F1 offspring were screened for ECFP-derived cyan eye fluorescence and line establishment was conducted as described above.

Whole-mount imaging

The imaging protocol was previously described[26]. Offspring from crosses between the homozygous AsteIr25a-QF2 driver line and the homozygous QUAS-mCD8:GFP effector line were screened for eye-specific expression of *DsRed* and *ECFP*. Antennae, maxillary palps, proboscis, and tarsi from 4-6-day-old adults were dissected into 4% formaldehyde in PBST (0.1% Triton X-100 in phosphate-buffered saline) and fixed on ice for 30 min. Samples were then washed 3× in PBST for 10 min each, transferred onto slides, and mounted in Antifade Mounting Medium (Beyotime, P0126). Confocal microscopy images at 1024 × 1024 pixel resolution were collected with an

Langtaosha (LTS) Preprint doi: https://doi.org/10.65215/LTSpreprints.2026.11.14.000387. This version posted November 14, 2026. The copyright holder for this preprint (which was not certified by peer review) is the author/funder. All Rights Reserved. No reuse allowed without permission.

LSM980 system (Zeiss). A laser wavelength of 488 nm was used to detect green fluorescent protein (GFP).

Electrophysiology

Single-sensillum recordings (SSR) were conducted as described in Liu et al.[81] Mutant and wild-type female mosquitoes 4 days after eclosion were anesthetized on ice for 2-3 min and mounted on a microscope slide (76 × 26 mm). The antennae or maxillary palps were fixed with double-sided tape to a coverslip resting on a small ball of dental wax to facilitate manipulation. Once mounted, the specimen was placed under a microscope (Nikon, Eclipse FN1) and the antenna was viewed at a high magnification (1000×). Two tungsten microelectrodes were sharpened in 10% KNO_2 at 10 V. The reference electrode, which was connected to ground, was inserted into the compound eye of the mosquito; the recording electrode was connected to the preamplifier (10×; SYNTECH) and inserted into the shaft of an olfactory sensillum to complete the electrical circuit for extracellular recording of ORN potentials[82]. Controlled manipulation of the electrodes was performed using a micromanipulator (Burleigh, PCS-6000). The preamplifier was connected to an analog-to-digital signal converter (SYNTECH, IDAC-4), which in turn was connected to a computer for signal recording and visualization in the software AutoSpike v5.1 (SYNTECH) Signals were recorded for 10 s starting 1 s before stimulation, and the action potentials were counted offline automatically with AutoSpike over a 500-ms period before and after stimulation. Spontaneous firing rates observed in the preceding 500 ms were subtracted from the total spike rates observed during the 500-ms stimulation, and counts were calculated in spikes/s.

Fifty compounds from different chemical classes were selected for SSR of antennal olfactory sensilla, and ten compounds were used for maxillary palps, which contain only a single type of sensilla, the capitate peg. Each compound was prepared in 100-fold dilution (v/v) with dimethyl sulfoxide (DMSO) or paraffin oil. For each dilution, a 10 µL portion was dispersed onto a filter paper strip (4 × 30 mm), which was then inserted into a Pasteur pipette to create the stimulus cartridge. A sample containing the solvent alone served as the control. The airflow across the antennae or palps was maintained constant at a 20 mL/s throughout the experiment. Purified and humidified air was delivered to the preparation through a glass tube (10-mm inner diameter) perforated by a small hole 10 cm from the end of the tube, into which the tip of the Pasteur pipette could be inserted. The stimulus was delivered to the sensilla by inserting the tip of the stimulus cartridge into this hole and diverting a portion of the air stream (0.5 L/min) through the stimulus cartridge for 500 ms using a stimulus controller (CS 55, SYNTECH). The distance between the end of the glass tube and the antennae/palps was ≤ 1 cm. The number of spikes/s was obtained by averaging the results for each sensillum/compound combination.

The electroantennogram (EAG) or electropalpogram (EPG) procedures followed previously described protocols[52] with minor modifications. Briefly, the head of an adult *An. stephensi* female was excised and mounted on an EAG/EPG platform equipped with two micromanipulators and a high-impedance AC/DC preamplifier (10×; SYNTECH). Chlorinated silver wires in glass capillaries filled with 0.1% KCl and 0.5% polyvinylpyrrolidone were used for both reference and recording electrodes. One antenna/palp with the tip cut was accommodated into the recording electrode. The airflow across the preparation was maintained constant at 20 mL/s, to which a stimulus pulse of 2 mL/s was delivered for 500 ms. Any change in antennal/palp

Langtaosha (LTS) Preprint doi: https://doi.org/10.65215/LTSpreprints.2026.11.14.000387. This version posted November 14, 2026. The copyright holder for this preprint (which was not certified by peer review) is the author/funder. All Rights Reserved. No reuse allowed without permission.

deflection induced by the stimuli or control puffs was recorded for 10 s. All compounds were dissolved in DMSO or paraffin oil to make a test solution of 10-fold dilution. An aliquot (10 μL) of a tested compound was loaded onto a filter paper strip (4 × 30 mm), which was immediately inserted into a Pasteur pipette for evaporation. The solvent alone (DMSO or paraffin oil) served as the control. The resulting signals were imported into a computer via a data acquisition controller (SYNTECH, IDAC-2). For each compound, EAG/EPG responses from 5 to 16 female mosquitoes were recorded. These recordings were analyzed using EAG software (Version 2.7; SYNTECH). The EAG response (ΔmV) to each test stimulus was calculated by subtracting the response elicited by the solvent from that elicited by the compound.

Fecundity assays

Larval development. Following a blood meal, female mosquitoes commence oviposition on the third day. L1 larvae that hatched synchronously within a 1-h window were selected and transferred individually to 96-well plates (one larva per well). Each well contained 1 mL of water, which was refreshed daily, and an appropriate amount of larval food was provided until pupation. Genotypes (wild-type, heterozygotes, and homozygotes) were distinguished by fluorescence-based screening. The duration from the L1 stage to pupation was recorded individually for each larva.

Pupation time. Individual *Drosophila* vials were prepared by adding 3 mL of water and inserting a single filter paper strip (2 cm × 5 cm). L4 larvae approaching pupation were transferred individually into the prepared vials and allowed to undergo eclosion. The exact pupation time of each larva was recorded. Each pupa was then monitored continuously until adult eclosion. Eclosion time was defined as the moment when the adult mosquito emerged from the pupal case. Pupal duration was calculated as the difference between eclosion time and pupation time, representing the interval from the initiation of pupation to complete adult emergence.

Adult longevity. Adult female mosquitoes that eclosed within a single 8-h window were collected and transferred into cages (15-25 females per cage). They were provided with 10% sucrose solution and maintained under standard rearing conditions. The number of dead females in each cage was recorded once daily at a consistent time point. A mosquito was considered dead when it met all of the following criteria: complete absence of spontaneous locomotor activity in the entire body, including legs, antennae, and wings, and no responsive movement following gentle external stimuli, such as gentle prodding with a soft brush or a gentle air puff. The assay was continued until all mosquitoes died. Adult longevity was calculated from the day of eclosion to the day of death.

Behavioral assays

Pre-experimental conditioning. 25 non-blood-fed females (3-7-day-old) were transferred to mosquito cages (25cm*25cm*25cm) and sucrose-starved for 6 h before behavioral assays. Distilled water was provided ad libitum during the starvation period.

Heat- pod attraction assay. The heating feeder (Hemotek, FU1) of a membrane feeding system (Hemotek, PS6) was calibrated to 37°C. The reservoir was filled with double-distilled water and hermetically sealed with Parafilm. The apparatus was pre-equilibrated until a stable temperature was reached. The feeder was then placed on top of the mosquito cage, and mosquito attraction behavior was recorded for 30 min using a camera positioned beneath the cage to provide a ventral view of the feeding unit. A

Langtaosha (LTS) Preprint doi: https://doi.org/10.65215/LTSpreprints.2026.11.14.000387. This version posted November 14, 2026. The copyright holder for this preprint (which was not certified by peer review) is the author/funder. All Rights Reserved. No reuse allowed without permission.

positive thermotactic event was defined as each entry of a mosquito proboscis into the pre-defined spatial perimeter of the reservoir. If the same mosquito entered the perimeter multiple times, each entry was counted as a separate event. The total number of positive thermotactic events (N_positive) and the total number of mosquitoes tested (N_total) were determined by video analysis. The thermal attraction index was calculated as:

Thermal attraction index = N_positive / N_total

CO_2 attraction assay. Mosquito behavioral responses to CO_2 were evaluated in a transparent cylindrical acrylic chamber (15 cm in diameter and 15 cm in height). Both openings of the chamber were covered with fine-mesh nylon gauze to permit ventilation while preventing mosquito escape. Mosquitoes were introduced into the chamber and allowed to acclimate. An inverted conical funnel was tightly fitted over the top of the chamber and connected to a CO_2 source.

After a 2 min habituation period, once the mosquitoes had become quiescent and were resting on the cylinder sides, CO_2 was delivered at a constant flow rate of 0.2 L/min. Mosquitoes that failed to become quiescent before CO_2 delivery were considered invalid and excluded from the analysis. The adjusted total number of mosquitoes (N_valid) was calculated by subtracting the number of invalid individuals from the initial total. Mosquito behavior was monitored for 5 min. A mosquito was scored as showing a positive activation response when it initiated flight accompanied by distinct orientation or exploratory movement toward the CO_2 source. The number of mosquitoes showing a positive activation response was recorded as N_positive. The activation index was calculated as:

CO_2 activation index = N_positive / N_valid

Murine host-seeking assay. The mouse and mosquitoes were separated by partitions with or without a barrier to prevent or allow blood feeding, respectively. For the with-barrier condition, an annular lid (height, 1 mm; outer diameter, 12 cm; inner diameter, 6.5 cm) was used. The inner annular region contained uniformly distributed square apertures, allowing volatile chemical cues from the mouse abdominal skin to diffuse while preventing direct skin contact and biting by mosquitoes. For the without-barrier condition, an aluminum foil partition containing a central circular aperture (4 cm in diameter) was used to selectively expose the abdominal skin of an anesthetized mouse.

In both conditions, each mouse was positioned ventral side down with its abdominal skin placed against the partition. The partition-mouse assembly was securely affixed to the top surface of the mosquito cage. Mosquito host-seeking and blood-feeding behaviors were video-recorded for 6 min.

A positive host-seeking event was defined as each entry of a mosquito proboscis into the exposed skin area over the mouse, followed by either sustained proboscis contact or the initiation of blood feeding. If the same mosquito entered the defined area multiple times, each occurrence was counted as a separate event. The total number of positive host-seeking events (N_positive) and the total number of mosquitoes tested (N_total) were determined by video analysis. The host attraction index was calculated as:

Host attraction index = N_positive / N_total

Human blood-feeding assay. A latex glove with a circular dorsal cutout (4 cm in diameter) was used to provide a restricted access area on a human hand. Two male

Langtaosha (LTS) Preprint doi: https://doi.org/10.65215/LTSpreprints.2026.11.14.000387. This version posted November 14, 2026. The copyright holder for this preprint (which was not certified by peer review) is the author/funder. All Rights Reserved. No reuse allowed without permission.

volunteers (30 and 35 years old, respectively) with no reported allergy to mosquito biting were recruited. The gloved hand was placed inside a mosquito cage, and mosquito activity was monitored for 6 min using a camera positioned 40 cm above the access area. A mosquito was scored as showing a positive blood-feeding attempt when its proboscis was inserted onto the exposed human hand and it attempted to penetrate the skin. If the same mosquito entered the defined skin area multiple times, each entry was counted as a separate event. The scoring of blood-feeding events was started one minute after the initiation of video filming, and a total of five minutes of video was examined. The host attraction index was calculated as:

Host attraction index = N_positive / N_total

Mating assay

The mating assay was carried out as previously described with minor modifications[26]. Females and males were separated by sex on day 1 after emergence to ensure that no mating occurred. Three-day-old females (15/bucket) and males (10/bucket) were then placed together in a rearing bucket and allowed to mate freely for 5 days. All surviving females were then collected, and their spermathecae were dissected under a compound microscope. The spermathecae were then placed in 1× PBS (Solarbio, P1022) containing 300 nM DAPI, and a coverslip was used to gently press and rupture the spermathecae to release sperm. Insemination status was assessed under a fluorescence microscope at 1000× magnification. The insemination rate was calculated as the number of inseminated females divided by the total number of females per bucket

Transcriptomic analysis

Female WT and *Ir25a*$^{-/-}$ mosquitoes aged 3–7 days were anesthetized and dissected on ice. The dissected antennae and maxillary palps were placed in 1 mL TRIzol (Invitrogen, 15596026) on ice, and then snap-frozen in liquid nitrogen and stored at -80°C until RNA extraction. Each sample contained tissue from at least 200 female mosquitoes. Three biological replicates were prepared for each genotype. Total RNA was extracted using the PureLink RNA Mini Kit (Invitrogen, 12183018A) following the manufacturer's instructions and subsequently sequenced by Tsingke Biotech (Shanghai, China). Libraries were prepared using the VAHTS Universal V6 RNA-seq Library Prep Kit for Illumina (Vazyme, NR604). The libraries were sequenced on an Illumina NovaSeq X Plus platform to generate 150 bp paired-end reads (PE150). RNA-seq data were trimmed with Cutadapt v5.2[83], and then mapped to the reference genome[84] (NCBI RefSeq assembly: GCF_013141755.1) using STAR v2.7.11b[85]. Reads per gene was calculated using featureCounts v2.1.1[86], and the normalization and differential gene expression analysis were performed with DESeq2[87].

Acknowledgments

We thank all members of the Feng Liu Lab at Shenzhen Bay Laboratory (SZBL) for their suggestions and comments, and the sequencing platform at SZBL for equipment and technical support. This work was supported by the National Natural Science Foundation of China (Grant No. 82372289 and 82561128263), and Guangdong Pearl River Funding (Grant No. 2023QN10Y093) awarded to F.L., Gates Foundations (INV-061480) awarded to Z.L., and Shenzhen Medical Academy of Research and Translation (SMART) (Grant No. A032400171) to S.T.F.; Guizhou Provincial Science and Technology Department (Grant No. Qian Ke He Ji Chu ZK [2024]

Langtaosha (LTS) Preprint doi: https://doi.org/10.65215/LTSpreprints.2026.11.14.000387. This version posted November 14, 2026. The copyright holder for this preprint (which was not certified by peer review) is the author/funder. All Rights Reserved. No reuse allowed without permission.

General 423) and Guizhou Provincial Grants for Higher Education Development (Grant No. 209-0325001) to Z.Y..

Author contributions

FL, ZY, STF, and ZL designed the research; ZY, GF, STF, DG, YW, XS, LZ and SL performed the research; ZY, STF, GF, DG, and FL analyzed the data; ZY, STF, GF, HZ, ZL, and FL wrote and edited the paper. All authors approved the manuscript.

Competing Interests

Authors declare that they have no competing interests.

Declarations

Ethics approval and consent to participate

All animals were handled strictly in accordance with the guidelines of the Care and Use of Laboratory Animals of the National Institutes of Health and the Office of Laboratory Animal Welfare, China. The research protocol was approved by the Institutional Animal Care and Use Committee at Shenzhen Bay Laboratory, China. This study was conducted in accordance with the research protocol reviewed and approved by the Medical Ethics Committee of Shenzhen Bay Laboratory (Approval No. YL 2026-018, Approval Date: Sep 28, 2026). Written informed consent was obtained from all participants prior to their inclusion in the study, and all personal identifiers were removed to protect participants' privacy.

Langtaosha (LTS) Preprint doi: https://doi.org/10.65215/LTSpreprints.2026.11.14.000387. This version posted November 14, 2026. The copyright holder for this preprint (which was not certified by peer review) is the author/funder. All Rights Reserved. No reuse allowed without permission.

References

1. McMeniman, C. J., Corfas, R. A., Matthews, B. J., Ritchie, S. A. & Vosshall, L. B. Multimodal integration of carbon dioxide and other sensory cues drives mosquito attraction to humans. *Cell* **156**, 1060–1071 (2014).
2. Morita, T. *et al.* Cross-modal sensory compensation increases mosquito attraction to humans. *Sci. Adv.* **11**, eadn5758 (2025).
3. Hawaria, D. *et al.* First report of Anopheles stephensi from southern Ethiopia. *Malar. J.* **22**, 373 (2023).
4. Acosta, A. L., Castro, M. C., Laporta, G. Z., Conn, J. E. & Sallum, M. A. M. Future global distribution and climatic suitability of Anopheles stephensi. *Sci. Rep.* **15**, 22268 (2025).
5. Liu, Q. *et al.* Possible potential spread of Anopheles stephensi, the Asian malaria vector. *BMC Infect. Dis.* **24**, 333 (2024).
6. Hansson, B. S. & Stensmyr, M. C. Evolution of insect olfaction. *Neuron* **72**, 698–711 (2011).
7. Keil, T. A. Comparative morphogenesis of sensilla: A review. *Int. J. Insect Morphol. Embryol.* **26**, 151–160 (1997).
8. Shanbhag, S. R., Müller, B. & Steinbrecht, R. A. Atlas of olfactory organs of Drosophila melanogaster 2. Internal organization and cellular architecture of olfactory sensilla. *Arthropod Struct. Dev.* **29**, 211–229 (2000).
9. Kim, M. S., Repp, A. & Smith, D. P. LUSH odorant-binding protein mediates chemosensory responses to alcohols in Drosophila melanogaster. *Genetics* **150**, 711–721 (1998).
10. Prelic, S. *et al.* Functional interaction between Drosophila olfactory sensory neurons and their support cells. *Front. Cell. Neurosci.* **15**, 789086 (2022).
11. Sen, A., Shetty, C., Jhaveri, D. & Rodrigues, V. Distinct types of glial cells populate the Drosophila antenna. *BMC Dev. Biol.* **5**, 25 (2005).
12. Konopka, J. K. *et al.* Olfaction in Anopheles mosquitoes. *Chem. Senses* **46**, bjab021 (2021).
13. Zhao, J., Chen, A. Q., Ryu, J. & del Mármol, J. Structural basis of odor sensing by insect heteromeric odorant receptors. *Science (80-.).* **384**, 1460–1467 (2024).
14. Butterwick, J. A. *et al.* Cryo-EM structure of the insect olfactory receptor Orco. *Nature* **560**, 447–452 (2018).
15. Carey, A. F., Wang, G., Su, C. Y., Zwiebel, L. J. & Carlson, J. R. Odorant reception in the malaria mosquito Anopheles gambiae. *Nature* **464**, 66–71 (2010).
16. Ma, D. *et al.* Structural basis for sugar perception by Drosophila gustatory receptors. *Science (80-.).* **383**, 1–15 (2024).
17. Lu, T. *et al.* Odor Coding in the Maxillary Palp of the Malaria Vector Mosquito Anopheles gambiae. *Curr. Biol.* **17**, 1533–1544 (2007).
18. Ni, L. The structure and function of ionotropic receptors in Drosophila. *Front.*

Langtaosha (LTS) Preprint doi: https://doi.org/10.65215/LTSpreprints.2026.11.14.000387. This version posted November 14, 2026. The copyright holder for this preprint (which was not certified by peer review) is the author/funder. All Rights Reserved. No reuse allowed without permission.

Mol. Neurosci. **13**, 638839 (2021).

19. Montell, C. Drosophila sensory receptors—A set of molecular swiss army knives. *Genetics* **217**, 1–34 (2021).

20. Herre, M. *et al.* Non-canonical odor coding in the mosquito. *Cell* **185**, 3104-3123.e28 (2022).

21. Task, D. *et al.* Chemoreceptor co-expression in Drosophila melanogaster olfactory neurons. *Elife* **11**, (2022).

22. Raji, J. I., Konopka, J. K. & Potter, C. J. A spatial map of antennal-expressed ionotropic receptors in the malaria mosquito. *Cell Rep.* **42**, 112101 (2023).

23. Fernández-Chiappe, F., Ocker, G. K. & Younger, M. A. Prospects on non-canonical olfaction in the mosquito and other organisms: why co-express? *Curr. Opin. Insect Sci.* **67**, 101291 (2025).

24. Goldman, O. V. *et al.* A single-nucleus transcriptomic atlas of the adult Aedes aegypti mosquito. *Cell* **188**, 7267-7290.e26 (2025).

25. Raji, J. I. *et al.* Aedes aegypti Mosquitoes Detect Acidic Volatiles Found in Human Odor Using the IR8a Pathway. *Curr. Biol.* **29**, 1253-1262.e7 (2019).

26. Ye, Z. *et al.* Discrete roles of Ir76b ionotropic coreceptor impact olfaction, blood feeding, and mating in the malaria vector mosquito Anopheles coluzzii. *Proc. Natl. Acad. Sci. U. S. A.* **119**, e2112385119 (2022).

27. Vulpe, A. & Menuz, K. Ir76b is a Co-receptor for Amine Responses in Drosophila Olfactory Neurons. *Front. Cell. Neurosci.* **15**, 759238 (2021).

28. Stanley, M., Ghosh, B., Weiss, Z. F., Christiaanse, J. & Gordon, M. D. Mechanisms of lactic acid gustatory attraction in Drosophila. *Curr. Biol.* **31**, 3525-3537.e6 (2021).

29. Lee, Y., Poudel, S., Kim, Y., Thakur, D. & Montell, C. Calcium taste avoidance in Drosophila. *Neuron* **97**, 67-74.e4 (2018).

30. McDowell, S. A. T., Stanley, M. & Gordon, M. D. A molecular mechanism for high salt taste in Drosophila. *Curr. Biol.* **32**, 3070-3081.e5 (2022).

31. Ahn, J.-E., Chen, Y. & Amrein, H. Molecular basis of fatty acid taste in Drosophila. *Elife* **6**, e30115 (2017).

32. Chen, C. *et al.* Drosophila ionotropic receptor 25a mediates circadian clock resetting by temperature. *Nature* **527**, 516–520 (2015).

33. Ni, L. *et al.* The ionotropic receptors IR21a and IR25a mediate cool sensing in Drosophila. *Elife* **5**, (2016).

34. Knecht, Z. A. *et al.* Ionotropic receptor-dependent moist and dry cells control hygrosensation in Drosophila. *Elife* **6**, e26654 (2017).

35. De Obaldia, M. E. *et al.* Differential mosquito attraction to humans is associated with skin-derived carboxylic acid levels. *Cell* **185**, 4099-4116.e13 (2022).

36. Shrestha, B., Sang, J., Rimal, S. & Lee, Y. Pharyngeal neuronal mechanisms governing sour taste perception in Drosophila melanogaster. *Elife* **13**, RP101439 (2024).

Langtaosha (LTS) Preprint doi: https://doi.org/10.65215/LTSpreprints.2026.11.14.000387. This version posted November 14, 2026. The copyright holder for this preprint (which was not certified by peer review) is the author/funder. All Rights Reserved. No reuse allowed without permission.

37. Qian, Q. *et al.* The influence of IR25a on electrophysiology and reproductive behaviour in the oriental fruit fly, Bactrocera dorsalis. *Insect Mol. Biol.* **35**, 1–13 (2026).

38. Omondi, B. A., Majeed, S. & Ignell, R. Functional development of carbon dioxide detection in the maxillary palp of Anopheles gambiae. *J. Exp. Biol.* **218**, 2482–2488 (2015).

39. Speth, Z. *et al.* Characterization of Anopheles stephensi odorant receptor 8, an abundant component of the mouthpart chemosensory transcriptome. *Insects* **12**, 593 (2021).

40. Potter, C. J., Tasic, B., Russler, E. V., Liang, L. & Luo, L. The Q system: A repressible binary system for transgene expression, lineage tracing, and mosaic analysis. *Cell* **141**, 536–548 (2010).

41. Campesan, S. *et al.* The kynurenine pathway modulates neurodegeneration in a Drosophila model of Huntington's disease. *Curr. Biol.* **21**, 961–966 (2011).

42. Mukabayire, O., Cornel, A. J., Dotson, E. M., Collins, F. H. & Besansky, N. J. The tryptophan oxygenase gene of Anopheles gambiae. *Insect Biochem. Mol. Biol.* **26**, 525–528 (1996).

43. Besansky, N. J. *et al.* The Anopheles gambiae tryptophan oxygenase gene expressed from a baculovirus promoter complements Drosophila melanogaster vermilion. *Insect Biochem. Mol. Biol.* **27**, 803–805 (1997).

44. Miller, S. W., Avidor-Reiss, T., Polyanovsky, A. & Posakony, J. W. Complex interplay of three transcription factors in controlling the tormogen differentiation program of Drosophila mechanoreceptors. *Dev. Biol.* **329**, 386–399 (2009).

45. Loh, L. S. *et al.* Lepidopteran scale cells derive from sensory organ precursors through a canonical lineage. *Development* **152**, DEV204501 (2025).

46. Ballou, S., Zlotnick, K., Tolmach, D. & Menuz, K. Identification of markers facilitating the study of support cells in adult olfactory sensilla in Drosophila. *Insect Biochem. Mol. Biol.* **195**, 104658 (2026).

47. Li, H. *et al.* Fly Cell Atlas: A single-nucleus transcriptomic atlas of the adult fruit fly. *Science (80-.).* **375**, eabk2432 (2022).

48. Sun, H., Liu, F., Ye, Z., Baker, A. & Zwiebel, L. J. Mutagenesis of the orco odorant receptor co-receptor impairs olfactory function in the malaria vector Anopheles coluzzii. *Insect Biochem. Mol. Biol.* **127**, (2020).

49. Degennaro, M. *et al.* Orco mutant mosquitoes lose strong preference for humans and are not repelled by volatile DEET. *Nature* **498**, 487–491 (2013).

50. Cooke, M. M., Chembars, M. S. & Pitts, R. J. The dysregulation of tuning receptors and transcription factors in the antennae of Orco and Ir8a mutants in Aedes aegypti suggests a chemoreceptor regulatory mechanism involving the MMB/dREAM complex. *Insects* **16**, 638 (2025).

51. Long, T., Mohapatra, P., Ballou, S. & Menuz, K. Odorant receptor co-receptors affect expression of tuning receptors in Drosophila. *Front. Cell. Neurosci.* **18**, 1390557 (2024).

52. Yao, H. *et al.* Unveiling the developmental dynamics and functional role of

Langtaosha (LTS) Preprint doi: https://doi.org/10.65215/LTSpreprints.2026.11.14.000387. This version posted November 14, 2026. The copyright holder for this preprint (which was not certified by peer review) is the author/funder. All Rights Reserved. No reuse allowed without permission.

Odorant Receptor Co-receptor (Orco) in Aedes albopictus: A novel mechanism for regulating odorant receptor expression. *PLoS Negl. Trop. Dis.* **19**, e0013753 (2025).

53. Benton, R., Vannice, K. S., Gomez-Diaz, C. & Vosshall, L. B. Variant ionotropic glutamate receptors as chemosensory receptors in Drosophila. *Cell* **136**, 149–162 (2009).

54. Croset, V. *et al.* Ancient protostome origin of chemosensory ionotropic glutamate receptors and the evolution of insect taste and olfaction. *PLoS Genet.* **6**, e1001064 (2010).

55. Ando, T. *et al.* Nanopore Formation in the Cuticle of an Insect Olfactory Sensillum. *Curr. Biol.* **29**, 1512-1520.e6 (2019).

56. Wang, Y. *et al.* CRISPR/Cas9 mediates efficient site-specific mutagenesis of the odorant receptor co-receptor (Orco) in the malaria vector Anopheles sinensis. *Pest Manag. Sci.* **78**, 3294–3304 (2022).

57. Riabinina, O. *et al.* Organization of olfactory centres in the malaria mosquito Anopheles gambiae. *Nat. Commun.* **7**, (2016).

58. Maekawa, E. *et al.* The role of proboscis of the malaria vector mosquito Anopheles stephensi in host-seeking behavior. *Parasites and Vectors* **4**, 10 (2011).

59. Greppi, C. *et al.* Mosquito heat seeking is driven by an ancestral cooling receptor. *Science (80-.).* **367**, 681–684 (2020).

60. Laursen, W. J. *et al.* Humidity sensors that alert mosquitoes to nearby hosts and egg-laying sites. *Neuron* **111**, 874-887.e8 (2023).

61. Keane, G. T. & Garrity, P. A. Mosquito heat and humidity detection in host seeking and oviposition behavior. *Curr. Opin. Neurobiol.* **99**, 103225 (2026).

62. Wang, G. *et al.* Anopheles gambiae TRPA1 is a heat-activated channel expressed in thermosensitive sensilla of female antennae. *Eur. J. Neurosci.* **30**, 967–974 (2009).

63. Corfas, R. A. & Vosshall, L. B. The cation channel TRPA1 tunes mosquito thermotaxis to host temperatures. *Elife* **4**, e11750 (2015).

64. Chandel, A. *et al.* Thermal infrared directs host-seeking behaviour in Aedes aegypti mosquitoes. *Nature* **633**, 615–623 (2024).

65. Liu, M. Z. & Vosshall, L. B. General visual and contingent thermal cues interact to elicit attraction in female Aedes aegypti mosquitoes. *Curr. Biol.* **29**, 2250-2257.e4 (2019).

66. Wolf, F. A., Angerer, P. & Theis, F. J. SCANPY: Large-scale single-cell gene expression data analysis. *Genome Biol.* **19**, 15 (2018).

67. Wolock, S. L., Lopez, R. & Klein, A. M. Scrublet: Computational identification of cell doublets in single-cell transcriptomic data. *Cell Syst.* **8**, 281-291.e9 (2019).

68. Pullin, J. M. & McCarthy, D. J. A comparison of marker gene selection methods for single-cell RNA sequencing data. *Genome Biol.* **25**, 56 (2024).

69. Blum, M., Hobbs, E., Florentino, L. & Bateman, A. InterProScan 6: a modern

Langtaosha (LTS) Preprint doi: https://doi.org/10.65215/LTSpreprints.2026.11.14.000387. This version posted November 14, 2026. The copyright holder for this preprint (which was not certified by peer review) is the author/funder. All Rights Reserved. No reuse allowed without permission.

large-scale protein function annotation pipeline. *Bioinforma. Adv.* **6**, vbag141 (2026).

70. Emms, D. M. & Kelly, S. OrthoFinder: Phylogenetic orthology inference for comparative genomics. *Genome Biol.* **20**, 238 (2019).

71. Mier, P. *et al.* Annotation and analysis of 3902 odorant receptor protein sequences from 21 insect species provide insights into the evolution of odorant receptor gene families in solitary and social insects. *Genes (Basel).* **13**, 919 (2022).

72. Mitchell, R. F., Moran, K. M. & McKenna, D. D. Early hexapod genomes reveal the deep origin of insect gustatory and odorant receptors. *Nat. Commun.* **17**, 6881 (2026).

73. Katoh, K. & Standley, D. M. MAFFT multiple sequence alignment software version 7: Improvements in performance and usability. *Mol. Biol. Evol.* **30**, 772–780 (2013).

74. Steenwyk, J. L., Buida, T. J., Li, Y., Shen, X. X. & Rokas, A. ClipKIT: A multiple sequence alignment trimming software for accurate phylogenomic inference. *PLoS Biol.* **18**, e3001007 (2020).

75. Kozlov, A. M., Darriba, D., Flouri, T., Morel, B. & Stamatakis, A. RAxML-NG: A fast, scalable and user-friendly tool for maximum likelihood phylogenetic inference. *Bioinformatics* **35**, 4453–4455 (2019).

76. Barbera, P. *et al.* EPA-ng: Massively parallel evolutionary placement of genetic sequences. *Syst. Biol.* **68**, 365–369 (2019).

77. Hammond, A. *et al.* A CRISPR-Cas9 gene drive system targeting female reproduction in the malaria mosquito vector Anopheles gambiae. *Nat. Biotechnol.* **34**, 78–83 (2016).

78. Labun, K. *et al.* CHOPCHOP v3: Expanding the CRISPR web toolbox beyond genome editing. *Nucleic Acids Res.* **47**, W171–W174 (2019).

79. Gratz, S. J. *et al.* Highly specific and efficient CRISPR/Cas9-catalyzed homology-directed repair in Drosophila. *Genetics* **196**, 961–971 (2014).

80. Matthews, B. J., Younger, M. A. & Vosshall, L. B. The ion channel ppk301 controls freshwater egg-laying in the mosquito aedes aegypti. *Elife* **8**, (2019).

81. Liu, F., Chen, L., Appel, A. G. & Liu, N. Olfactory responses of the antennal trichoid sensilla to chemical repellents in the mosquito, Culex quinquefasciatus. *J. Insect Physiol.* **59**, 1169–1177 (2013).

82. Den Otter, C. J., Behan, M. & Maes, F. W. Single cell responses in female Pieris brassicae (Lepidoptera: Pieridae) to plant volatiles and conspecific egg odours. *J. Insect Physiol.* **26**, 465–472 (1980).

83. Martin, M. Cutadapt removes adapter sequences from high-throughput sequencing reads. *EMBnet.journal* **17**, 10 (2011).

84. Chakraborty, M. *et al.* Hidden genomic features of an invasive malaria vector, Anopheles stephensi, revealed by a chromosome-level genome assembly. *BMC Biol.* **19**, 28 (2021).

85. Dobin, A. *et al.* STAR: Ultrafast universal RNA-seq aligner. *Bioinformatics* **29**,

Langtaosha (LTS) Preprint doi: https://doi.org/10.65215/LTSpreprints.2026.11.14.000387. This version posted November 14, 2026. The copyright holder for this preprint (which was not certified by peer review) is the author/funder. All Rights Reserved. No reuse allowed without permission.

15–21 (2013).

86. Liao, Y., Smyth, G. K. & Shi, W. featureCounts: An efficient general purpose program for assigning sequence reads to genomic features. *Bioinformatics* **30**, 923–930 (2014).

87. Love, M. I., Huber, W. & Anders, S. Moderated estimation of fold change and dispersion for RNA-seq data with DESeq2. *Genome Biol.* **15**, 550 (2014).

Langtaosha (LTS) Preprint doi: https://doi.org/10.65215/LTSpreprints.2026.11.14.000387. This version posted November 14, 2026. The copyright holder for this preprint (which was not certified by peer review) is the author/funder. All Rights Reserved. No reuse allowed without permission.

Figures

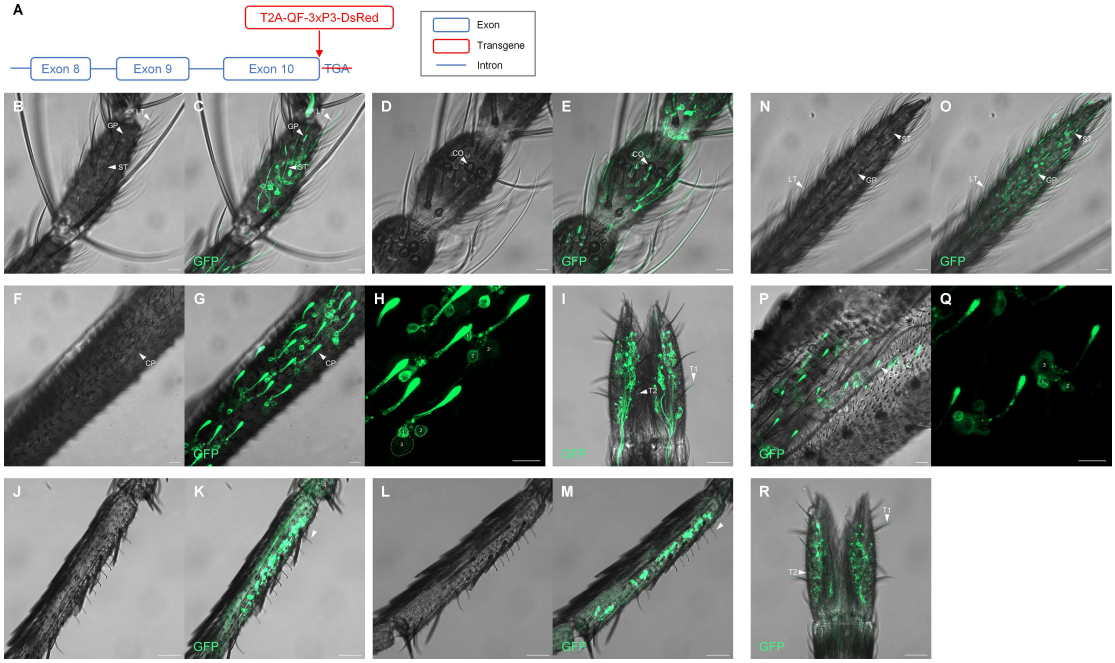


Figure 1. Localization of AsteIr25a in chemosensory appendages. **(A)** Schematic of AsteIr25a-QF2 driver line. A 'T2A-QF2-3×P3-DsRed' cassette was inserted into exon 10 to replace the stop codon. **(B, C)** Representative bright-field image **(B)** with GFP fluorescence overlay confocal Z-projections **(C)** of the 11th flagellomere on a whole-mount female antenna. GFP-labeled long trichoid (LT), short trichoid (ST), and grooved peg (GP) were highlighted by arrows. **(D, E)** Representative bright-field image **(D)** with GFP fluorescence overlay confocal Z-projections **(E)** of the 3rd flagellomere on a whole-mount female antenna. A GFP-labeled coeloconic sensillum (CO) was highlighted by an arrow. **(F, G)** Representative bright-field image **(F)** with GFP fluorescence overlay confocal Z-projections **(G)** of the 3rd segment on a whole-mount female maxillary palp. A GFP-labeled capitate peg (CP) was highlighted by an arrow. **(H)** An enlarged view of green fluorescence in **(G)** indicating that *Ir25a* is expressed in all three neurons innervating a capitate peg (circled by dashed lines and labeled by numbers). **(I)** Representative confocal Z-projection of a whole-mount female labellum. T1 and T2 sensilla were highlighted by arrows. **(J, K)** Representative bright-field image **(J)** with GFP fluorescence overlay confocal Z-projections **(K)** of the 3rd tarsomere on a whole-mount female protarsus. A GFP-labeled sensillum is highlighted by an arrow. **(L, M)** Representative bright-field image **(L)** with GFP fluorescence overlay confocal Z-projections **(M)** of the 4th tarsomere on a whole-mount female protarsus. A GFP-labeled sensillum is highlighted by an arrow. **(N, O)** Representative bright-field image **(N)** with GFP fluorescence overlay confocal Z-projections **(O)** of the 12th flagellomere on a whole-mount male antenna. GFP-labeled long trichoid (LT), short trichoid (ST), and grooved peg (GP) were highlighted by arrows. **(P)** Representative confocal Z-projection of the 4th segment on a whole-mount male maxillary palp. A GFP-labeled capitate peg (CP) was highlighted by an arrow. **(Q)** An enlarged view of green fluorescence in **(P)** indicating Ir25a is expressed in all three neurons innervating a capitate peg (labeled by numbers). **(R)** Representative confocal Z-projection of a whole-mount male labellum. T1 and T2 sensilla were highlighted by arrows. Scale bars: Antennae and maxillary palps, 10μm; Labella and tarsi, 30μm.

Langtaosha (LTS) Preprint doi: https://doi.org/10.65215/LTSpreprints.2026.11.14.000387. This version posted November 14, 2026. The copyright holder for this preprint (which was not certified by peer review) is the author/funder. All Rights Reserved. No reuse allowed without permission.

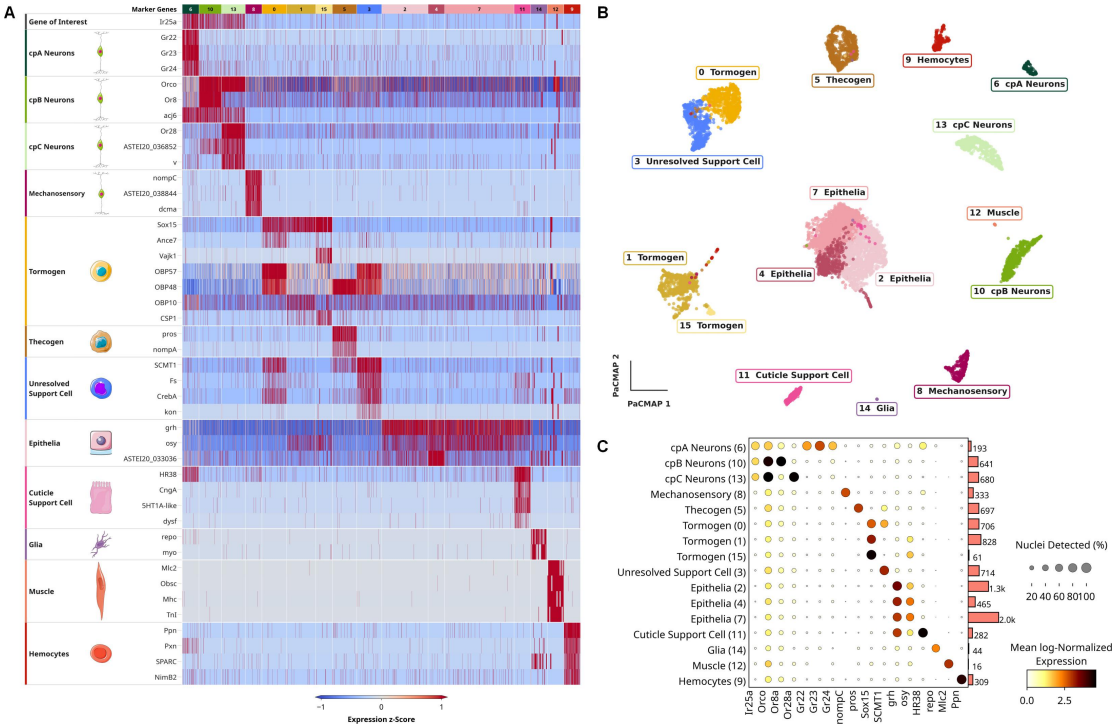


Figure 2. Single-nucleus profiling resolves neuronal and non-neuronal populations in the female maxillary palp. Single-nucleus RNA sequencing of one biological preparation of female *An. stephensi* maxillary palps yielded 9,268 retained nuclei, partitioned into 16 clusters using a 50-neighbor graph and Leiden resolution 0.70. **(A)** Curated marker-gene heatmap, with genes arranged in blocks corresponding to the indicated cluster identities and individual nuclei arranged by cluster. Ir25a is displayed separately in the top row. Expression was normalized to 10,000 counts per nucleus, natural-log-transformed using log1p, and standardized independently for each gene across all nuclei. Colors indicate expression z-scores, with the display saturated below −1 and above +1. Colored header bars identify clusters, while left-hand bars and cartoons denote the proposed cell-type groupings. Small clusters have expanded column widths for visibility, so block width is not a direct measure of abundance. Cartoons are schematic and do not depict experimentally established morphology. **(B)** PaCMAP embedding of the same nuclei, colored by cluster and labeled with cluster numbers and annotations. **(C)** Dotplot of selected cell-identity markers. Dot area is proportional to the percentage of nuclei in each cluster containing at least one unique molecular identifier (UMI) for the indicated gene. Dot color represents mean log-normalized expression across all nuclei in that cluster, including zero-count nuclei. Horizontal bars and accompanying numbers on the right indicate recovered cluster sizes.

Langtaosha (LTS) Preprint doi: https://doi.org/10.65215/LTSpreprints.2026.11.14.000387. This version posted November 14, 2026. The copyright holder for this preprint (which was not certified by peer review) is the author/funder. All Rights Reserved. No reuse allowed without permission.

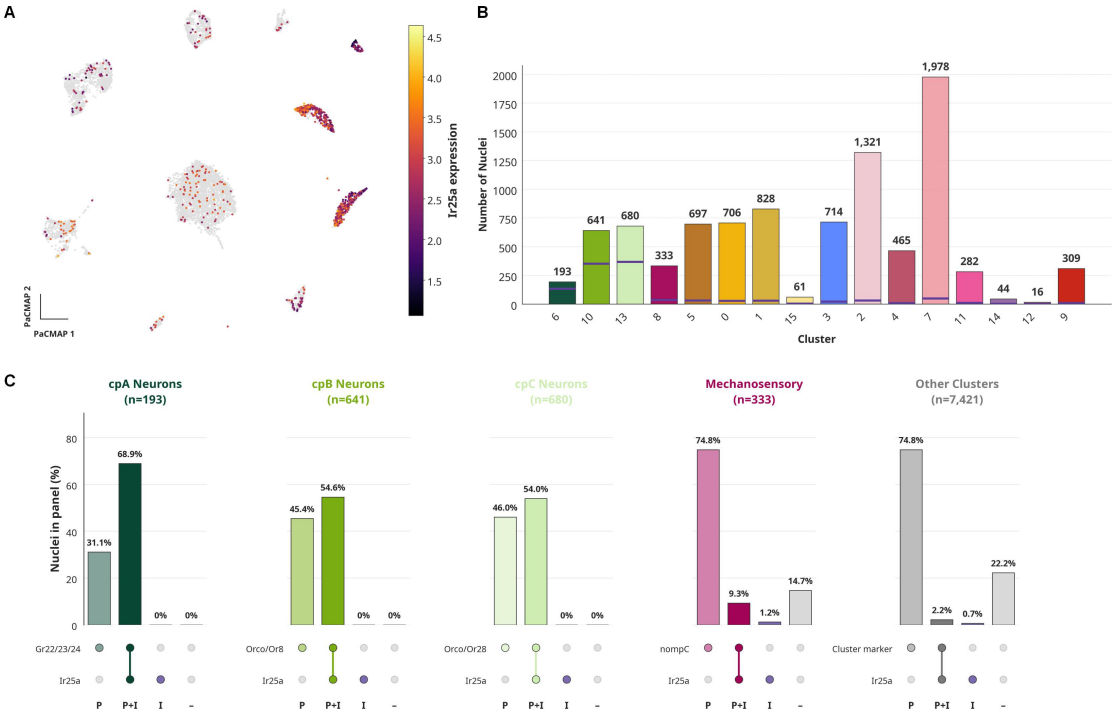


Figure 3. Ir25a transcript detection and co-detection across palpal cell populations. **(A)** Ir25a feature plot for ASTEI20_043271 on the same PaCMAP embedding used in Figure 2B. Nuclei with detected expression are colored by log-normalized transcript abundance; nuclei without detected expression are gray. **(B)** Total nuclei in each cluster, shown as bars colored consistently with Figure 2B. Numbers above bars give cluster sizes. The purple horizontal line spanning each bar marks the number of nuclei containing at least one Ir25a UMI. **(C)** UpSet-style co-detection summary for putative cpA neurons (cluster 6; n = 193), cpB neurons (cluster 10; n = 641), cpC neurons (cluster 13; n = 680), mechanosensory neurons (cluster 8; n = 333), and all remaining clusters pooled (n = 7,421). Detection was defined as at least one UMI in the counts matrix. Comparison signatures required any of Gr22/Gr23/Gr24 for cpA, Orco or Or8 for cpB, and Orco or Or28 for cpC. The mechanosensory comparison used nompC. In the pooled "Other Clusters" panel, each nucleus was tested against the rank-1 Wilcoxon marker of its own assigned cluster. P denotes the comparison signature or marker without detected Ir25a; P+I denotes both; I denotes Ir25a without the comparison signature or marker; and "–" denotes neither. Colored dots in the membership matrix indicate detection, and pale-gray dots indicate non-detection under these definitions; connected colored dots indicate co-detection.

Langtaosha (LTS) Preprint doi: https://doi.org/10.65215/LTSpreprints.2026.11.14.000387. This version posted November 14, 2026. The copyright holder for this preprint (which was not certified by peer review) is the author/funder. All Rights Reserved. No reuse allowed without permission.

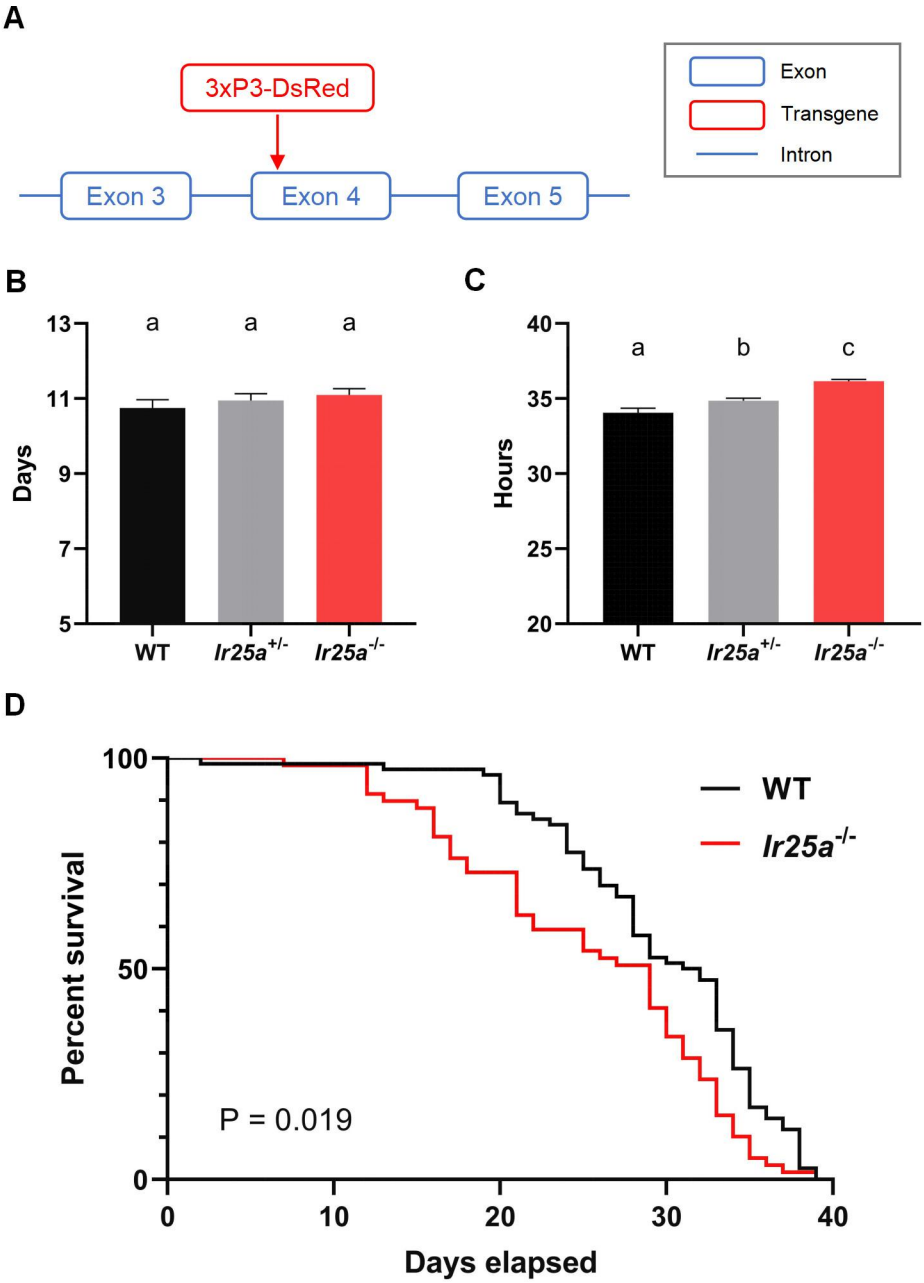
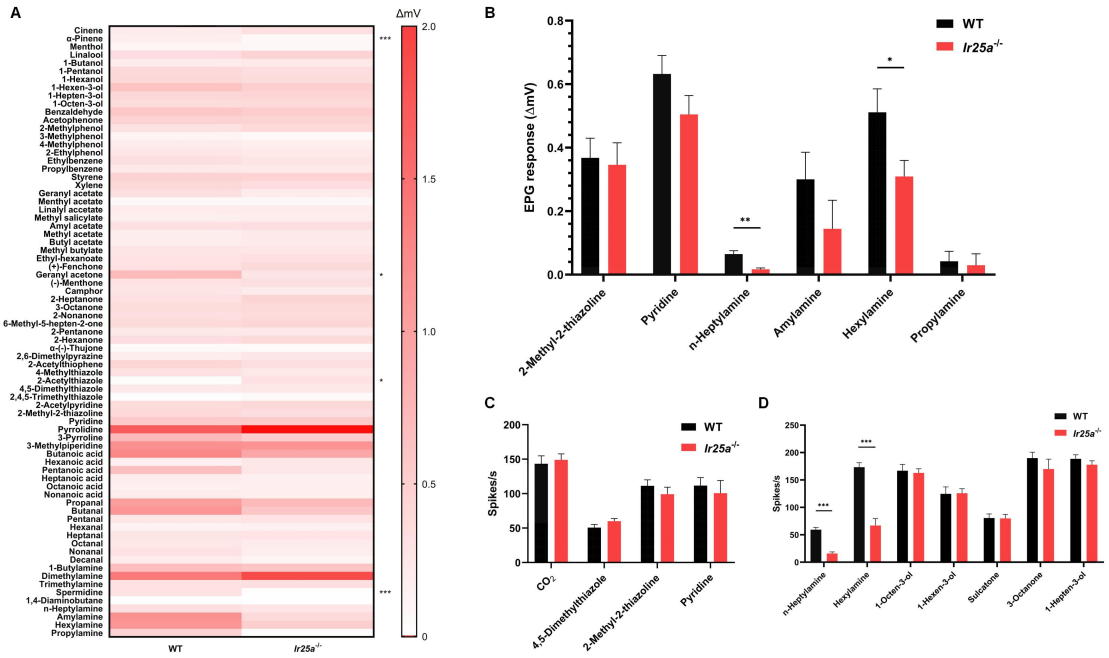


Figure 4. Development and survival curve of Ir25a null mutants. **(A)** Schematic of AsteIr25a null mutant line. A 3×P3-DsRed fluorescence marker was inserted into Exon 4 of AsteIr25a. **(B)** Larval development time of wild-type (WT), Ir25a heterozygous mutants ($Ir25a^{+/-}$), and Ir25a homozygous mutants ($Ir25a^{-/-}$). One-way ANOVA suggests no significant differences between the three genotypes (n = 12-21). **(C)** Duration of the pupal stage. One-way ANOVA suggests significant differences between the three genotypes. Different lowercase letters denote statistically significant differences (n = 12-27; P value < 0.05). **(D)** Survival curve of WT and *Ir25a*$^{-/-}$ females. Log-rank test suggests significant differences between the two genotypes (P value = 0.019). Error bars = SEM.

Langtaosha (LTS) Preprint doi: https://doi.org/10.65215/LTSpreprints.2026.11.14.000387. This version posted November 14, 2026. The copyright holder for this preprint (which was not certified by peer review) is the author/funder. All Rights Reserved. No reuse allowed without permission.



1429

1430 **Figure 5.** Electrophysiological responses of *An. stephensi* females. **(A)** EAG
1431 responses. The heatmap shows mean response amplitudes (ΔmV) of WT and *Ir25a*$^{-/-}$
1432 females to a panel of odorants. Asterisks denote significant differences between
1433 genotypes for each odorant determined by multiple t-tests using Holm-Sidak method:
1434 P value < 0.05 (*); P value < 0.001 (***). **(B)** EPG responses. An unpaired t-test
1435 suggests n-heptylamine and hexylamine elicited significantly reduced responses in
1436 *Ir25a*$^{-/-}$ females. **(C)** SSR responses of cpA neurons in capitate pegs. An unpaired t-
1437 test suggests no significant differences between the two genotypes. **(D)** SSR responses
1438 of cpB/C neurons in capitate pegs. An unpaired t-test suggests n-heptylamine and
1439 hexylamine elicited significantly reduced responses in *Ir25a*$^{-/-}$ females. Significance
1440 levels are depicted with asterisks: P value < 0.05 (*); P value < 0.01 (**); P value <
1441 0.001 (***). Error bars = SEM.

1442

Langtaosha (LTS) Preprint doi: https://doi.org/10.65215/LTSpreprints.2026.11.14.000387. This version posted November 14, 2026. The copyright holder for this preprint (which was not certified by peer review) is the author/funder. All Rights Reserved. No reuse allowed without permission.

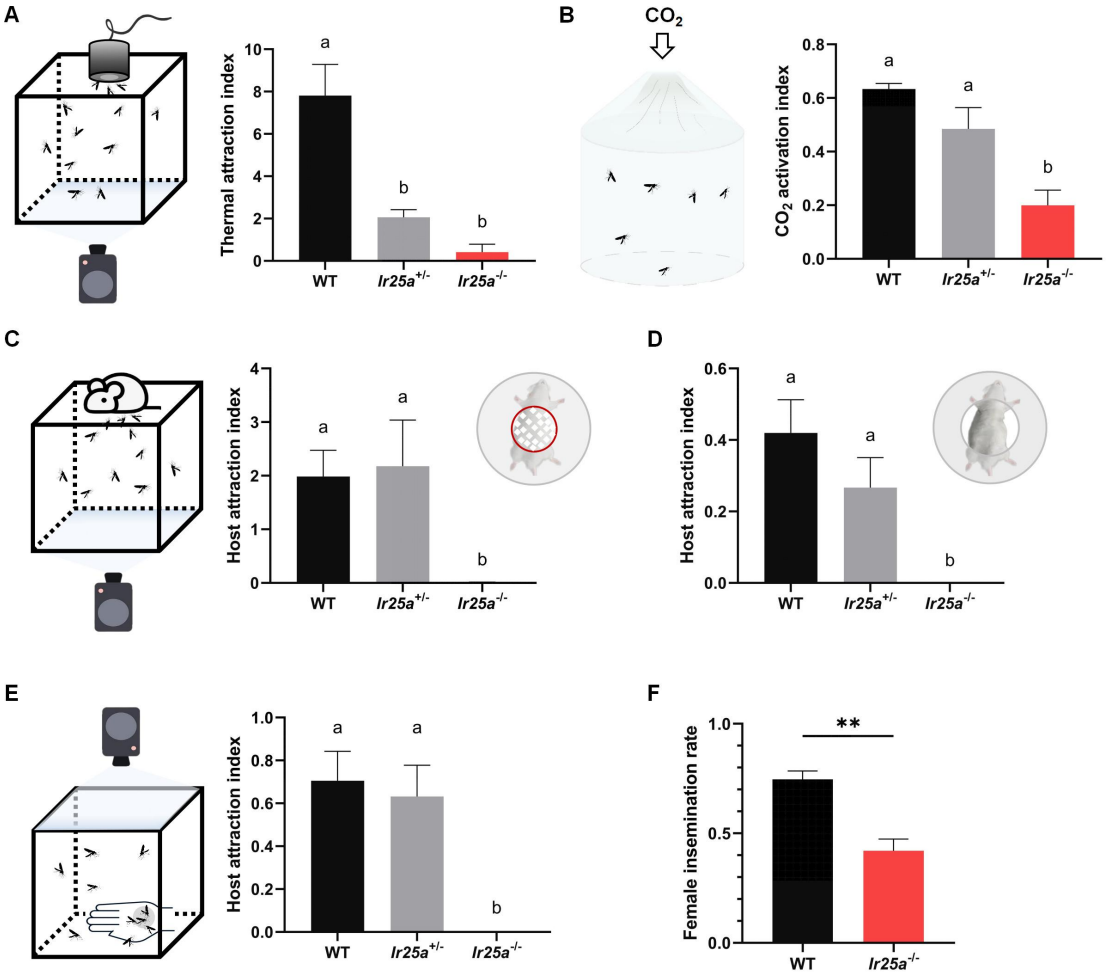
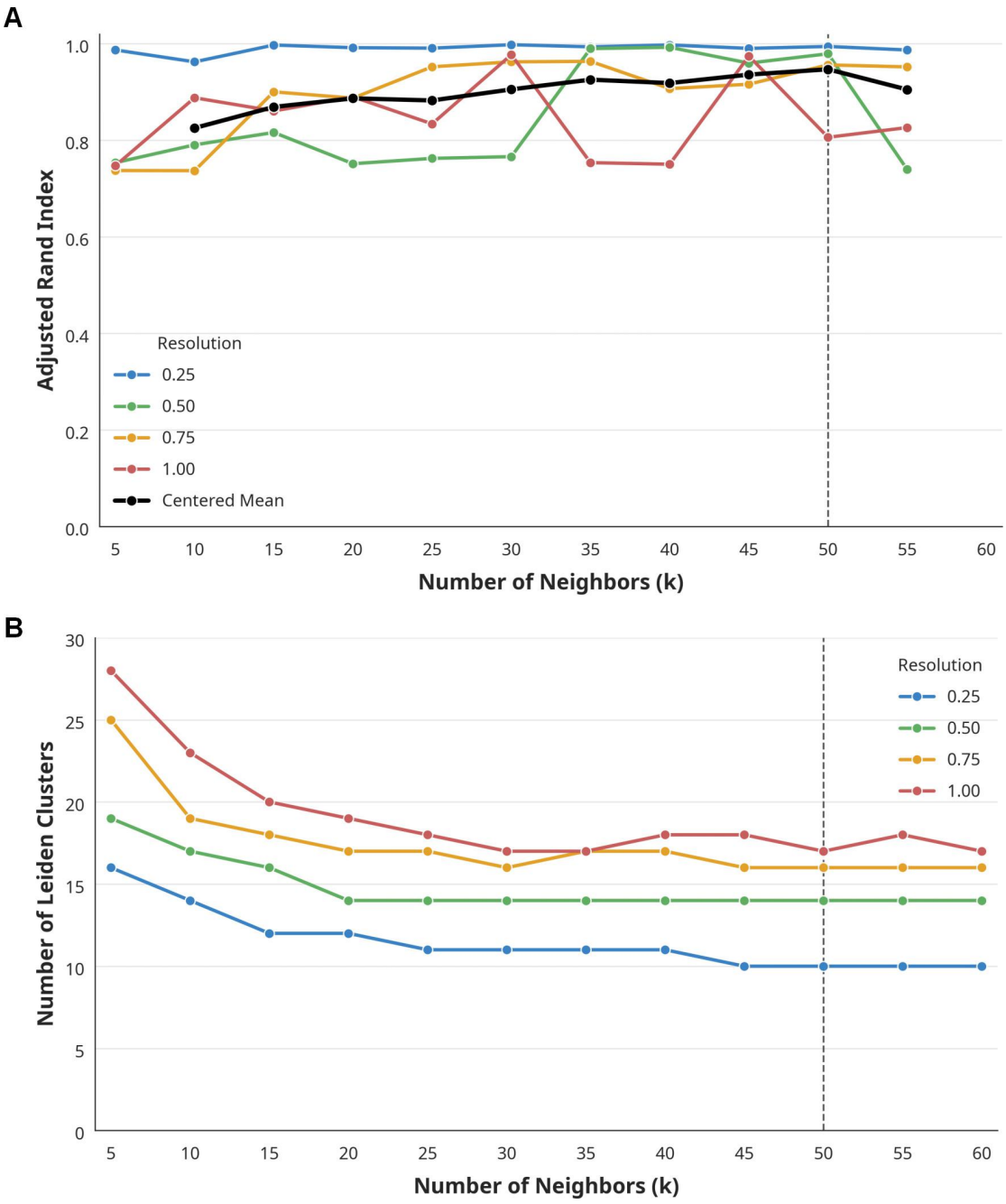


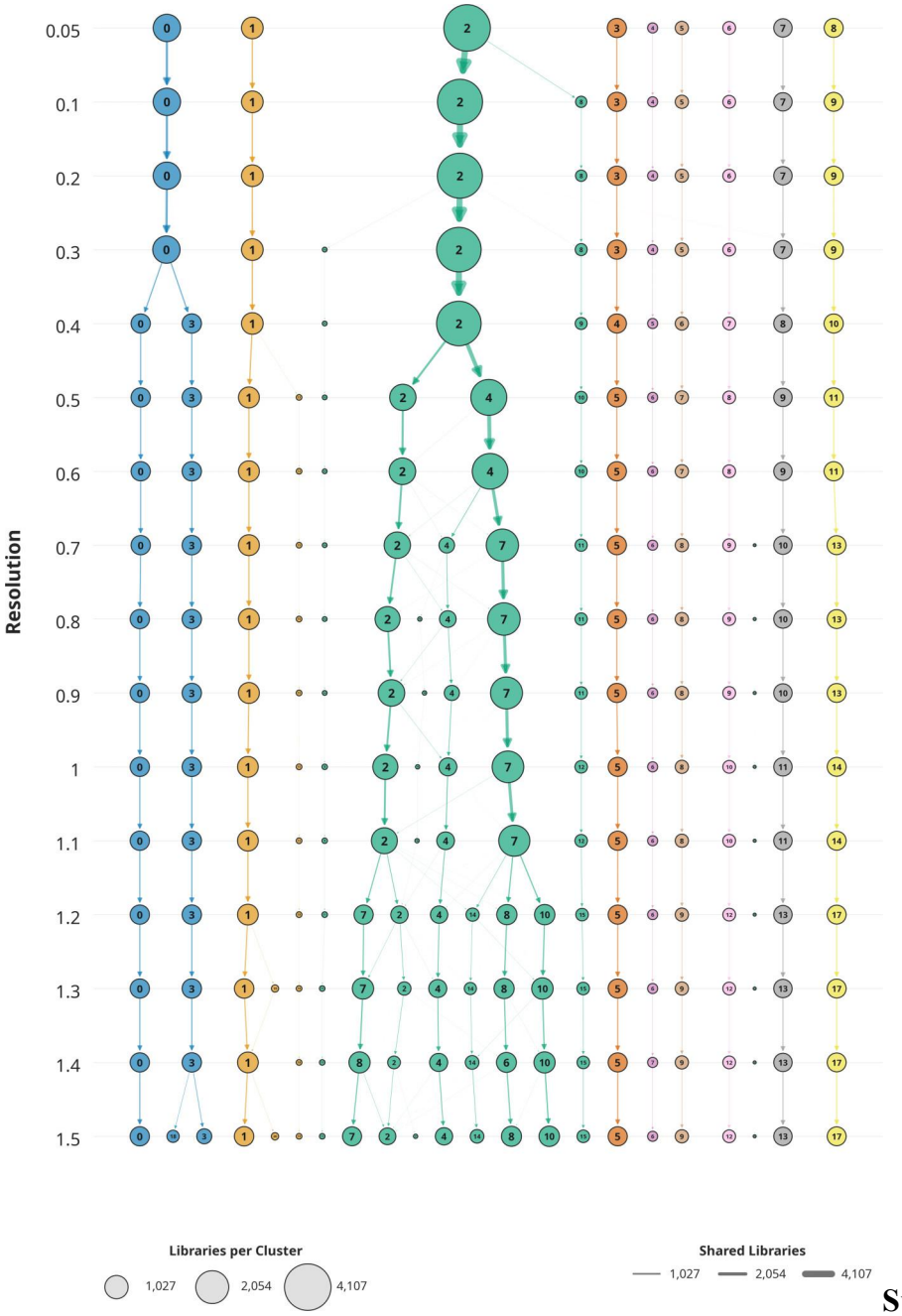
Figure 6. Behavioral assessment of *An. stephensi* females. **(A)** Schematic of the heat-pod attraction assay (left) and thermal attraction indexes (right). One-way ANOVA suggests that both Ir25a$^{+/-}$ and *Ir25a*$^{-/-}$ showed significantly reduced responses to the heat source. Different lowercase letters denote statistically significant differences (n = 4-5; P value < 0.05). **(B)** Schematic of CO_2 activation assay (left) and CO_2 activation indexes (right). One-way ANOVA suggests *Ir25a*$^{-/-}$ showed significantly reduced responses to CO_2. Different lowercase letters denote statistically significant differences (n = 6; P value < 0.05). **(C)** Schematic of the host-seeking assay using mice as the odor source with a barrier (left) and host attraction indexes (right). One-way ANOVA suggests *Ir25a*$^{-/-}$ showed significantly reduced host-seeking activity toward mice. Different lowercase letters denote statistically significant differences (n = 5; P value < 0.05). **(D)** Schematic of the host-seeking assay using mice as the odor source without a barrier (left) and host attraction indexes (right). One-way ANOVA suggests *Ir25a*$^{-/-}$ showed significantly reduced host-seeking activity toward mice. Different lowercase letters denote statistically significant differences (n = 4-6; P value < 0.05). **(E)** Schematic of the host-seeking assay using human hand as the odor source (left) and host attraction indexes (right). One-way ANOVA suggests *Ir25a*$^{-/-}$ showed significantly reduced host-seeking activity toward human hand. Different lowercase letters denote statistically significant differences (n = 4-6; P value < 0.05). **(F)** Female insemination rate in the mating assay. An unpaired t-test suggests a significant reduction in copulation between *Ir25a*$^{-/-}$ males and females (n = 4-5; P value < 0.01). Error bars = SEM.

Langtaosha (LTS) Preprint doi: https://doi.org/10.65215/LTSpreprints.2026.11.14.000387. This version posted November 14, 2026. The copyright holder for this preprint (which was not certified by peer review) is the author/funder. All Rights Reserved. No reuse allowed without permission.



Supplementary Figure S1. Sensitivity of Leiden clustering to neighborhood size. Neighborhood graphs were evaluated for $k = 5$–60 in increments of 5, with Leiden clustering at resolutions 0.25, 0.50, 0.75, and 1.00, using the same 9,268 nuclei and PCA representation. **(A)** Adjusted Rand index (ARI) comparing partitions at the same resolution between adjacent neighborhood sizes. Each colored point at k represents agreement between the partitions obtained with k and $k + 5$ neighbors; for example, the point at $k = 45$ compares $k = 45$ with $k = 50$. The black line shows the centered mean for each interior k, calculated by averaging comparisons with both adjacent tested neighborhood sizes across all four resolutions—eight ARIs per point. Centered means are not plotted at $k = 5$ or $k = 60$ because a comparison on one side is unavailable. **(B)** Number of Leiden clusters obtained at each neighborhood size. Dashed vertical lines in both panels mark the selected $k = 50$, which had the highest centered mean ARI among the tested values.

Langtaosha (LTS) Preprint doi: https://doi.org/10.65215/LTSpreprints.2026.11.14.000387. This version posted November 14, 2026. The copyright holder for this preprint (which was not certified by peer review) is the author/funder. All Rights Reserved. No reuse allowed without permission.



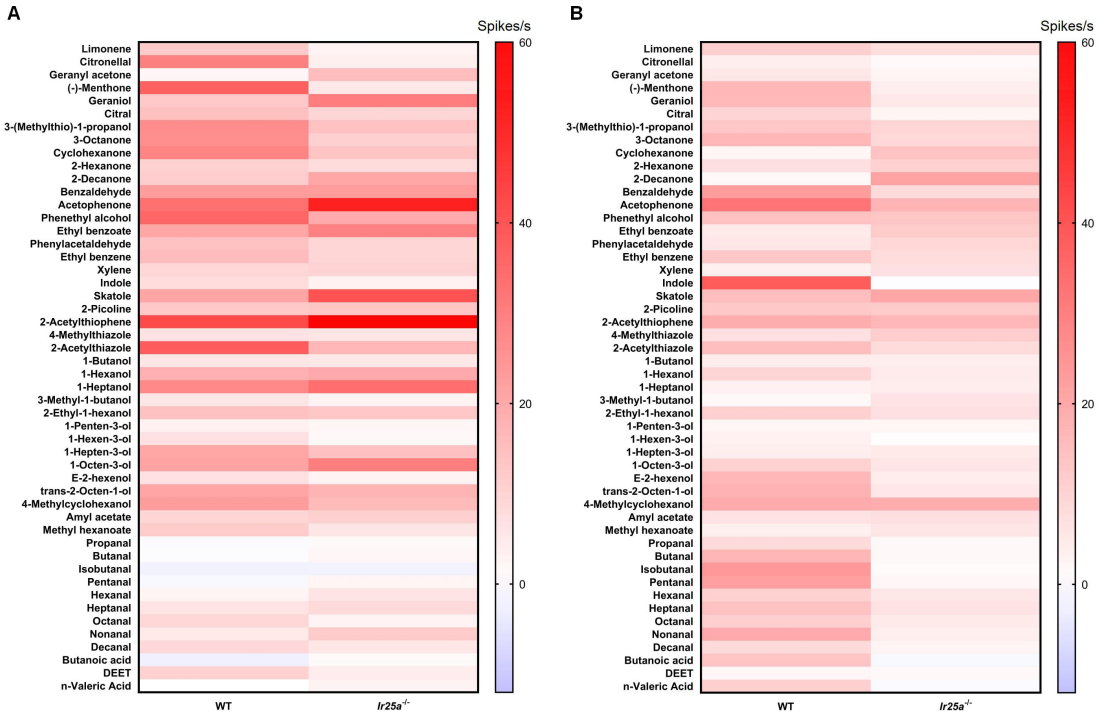
Supplementary Figure S2. Cross-resolution membership relationships among palpal transcriptomic clusters. Leiden clustering was performed on the fixed $k = 50$ graph at resolution 0.05 and at resolutions 0.10–1.50 in increments of 0.10. Rows are equally spaced and ordered from lower to higher resolution. Each circle represents a cluster; its area is proportional to the number of nuclei, and its internal label gives the cluster identifier at that resolution. Arrows connect clusters in adjacent rows that share nuclei, with arrow width proportional to the number of shared nuclei. Node colors identify the cluster at resolution 0.05 with which each node shares the largest number of nuclei. Cluster labels are local to each resolution; matching numbers in different rows do not necessarily identify the same population. Resolution 0.70, yielding 16 clusters, was retained for the main analyses after considering membership patterns together with marker profiles.

Langtaosha (LTS) Preprint doi: https://doi.org/10.65215/LTSpreprints.2026.11.14.000387. This version posted November 14, 2026. The copyright holder for this preprint (which was not certified by peer review) is the author/funder. All Rights Reserved. No reuse allowed without permission.

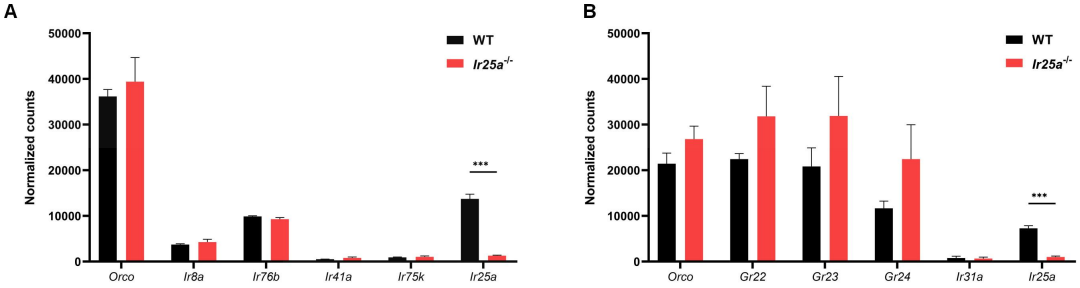


Supplementary Figure S3. Sparse detection of the candidate artichoke-associated gene in the female palp. Feature PaCMAP showing expression of the predicted *artichoke* (*atk*) ortholog ASTEI20_044372. Nuclei with detected transcripts are colored by log-normalized expression, while nuclei without detected transcripts are gray. At least one *atk* UMI was detected in only two nuclei (0.022%), providing no discernible population-level expression pattern for trichogen annotation.

Langtaosha (LTS) Preprint doi: https://doi.org/10.65215/LTSpreprints.2026.11.14.000387. This version posted November 14, 2026. The copyright holder for this preprint (which was not certified by peer review) is the author/funder. All Rights Reserved. No reuse allowed without permission.

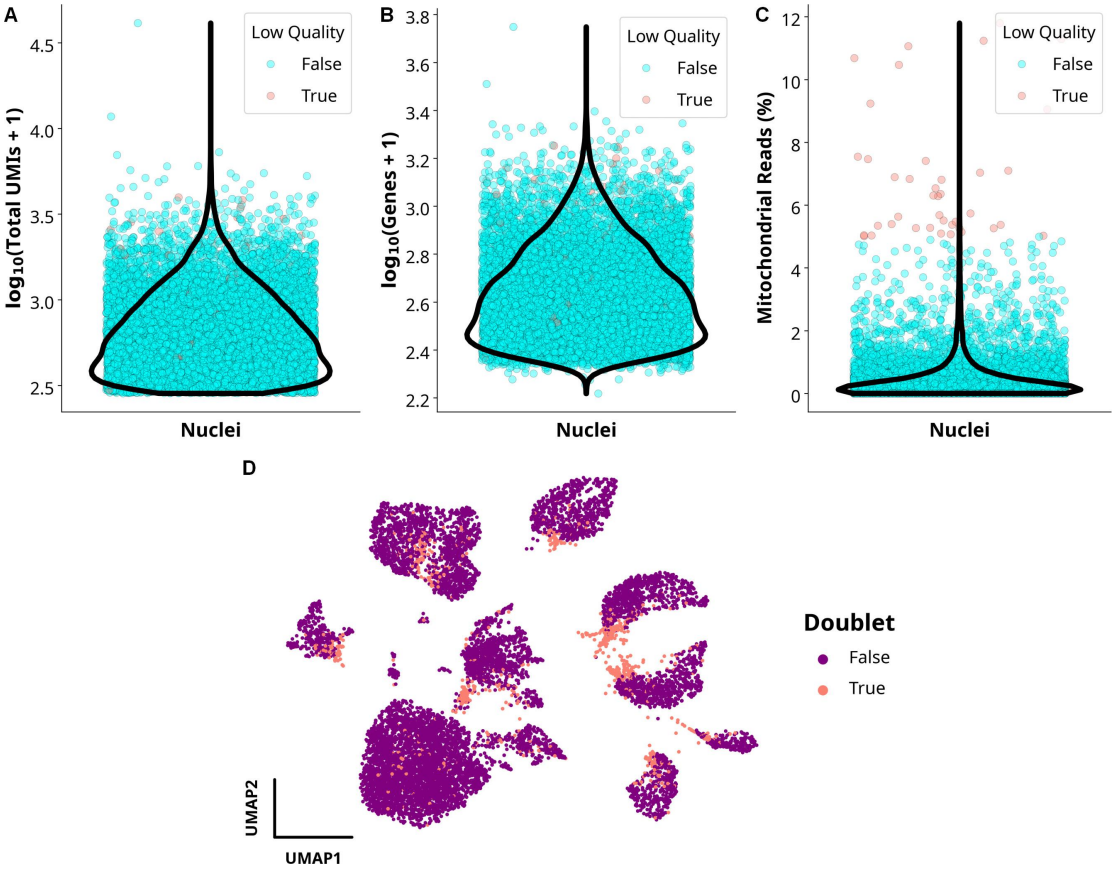


Supplementary Figure S4. SSR responses. The heatmap shows mean response amplitudes (spikes/s) of SBT **(A)** and SST **(B)** in WT and *Ir25a*$^{-/-}$ females to a panel of odorants. Multiple t-tests using Holm-Sidak method suggest no significant difference between WT and *Ir25a*$^{-/-}$ females.



Supplementary Figure S5. Normalized counts of selected chemosensory gene transcripts in antennae **(A)** and maxillary palps **(B)**. Differential expression analysis by DESeq2 suggests no significant differences in chemosensory gene transcript abundance between WT and *Ir25a*$^{-/-}$ females, but *Ir25a* (n = 3; P < 0.001). Error bars = SEM.

Langtaosha (LTS) Preprint doi: https://doi.org/10.65215/LTSpreprints.2026.11.14.000387. This version posted November 14, 2026. The copyright holder for this preprint (which was not certified by peer review) is the author/funder. All Rights Reserved. No reuse allowed without permission.



Supplementary Figure S6. Quality control and predicted-doublet filtering of the female palp single-nucleus dataset. **(A–C)** Distributions of $\log_{10}$ (total UMIs + 1), $\log_{10}$ (number of detected genes + 1), and the percentage of UMIs assigned to mitochondrial genes, respectively, across 10,175 input nucleus-associated barcodes. Each point represents one barcode. Outlined violins summarize the distributions. Cyan points passed the library-quality criteria, whereas salmon points were flagged by at least one criterion. Lower-tail cutoffs for total UMIs and detected genes were defined as three normal-consistency-scaled median absolute deviations below their medians on the $\log_2$ scale. Mitochondrial UMI fractions exceeding 5% also triggered exclusion. These criteria removed 40 barcodes. **(D)** UMAP of the 10,135 remaining barcodes before doublet removal, colored by Scrublet classification ("True," predicted doublet; "False," not predicted as a doublet). Removal of 867 predicted doublets left 9,268 nuclei for downstream analysis.

Langtaosha (LTS) Preprint doi: https://doi.org/10.65215/LTSpreprints.2026.11.14.000387. This version posted November 14, 2026. The copyright holder for this preprint (which was not certified by peer review) is the author/funder. All Rights Reserved. No reuse allowed without permission.

Supplementary Data 1. Cluster-wise marker rankings and comparative gene annotations for female maxillary palp nuclei. Workbook containing top-ranked marker genes and associated annotation evidence. Genes were ranked by one-versus-rest Wilcoxon score, and the top 50 genes per cluster were retained. Each row represents a cluster–gene entry, and a gene can occur in more than one cluster's marker list. Marker_Rank gives the within-cluster rank, Marker_Score the signed Wilcoxon score, and Marker_Log2FC the approximate $\log_2$ -fold-change estimate returned by Scanpy. Marker_Pct_In and Marker_Pct_Rest contain detection fractions for the focal cluster and all other nuclei, respectively. Annotation fields retain the original *A. stephensi* gene identifier, feature type, available names and descriptions, linked protein identifiers, InterPro/Pfam/PANTHER annotations and GO terms from InterProScan, and OrthoFinder orthogroup and pairwise-orthology information for *An. gambiae*, *Ae. aegypti*, and *D. melanogaster*. Where available, EPA-ng placement evidence includes the reference collection, placed protein identifiers, nearest-reference annotations, and likelihood weight ratios (LWRs). Missing annotation fields are denoted NA.

Supplementary Data 2. List of oligonucleotide sequences for vector constructions and validations.